The Astronomical Journal, 165:6 (32pp), 2023 January https://doi.org/10.3847/1538-3881/ac9c59
© 2022. The Author(s). Published by the American Astronomical Society.
OPEN ACCESS

Evolved Eclipsing Binaries and the Age of the Open Cluster NGC 752*

Eric L. Sandquist[1], Andrew J. Buckner[1], Matthew D. Shetrone[2,3], Samuel C. Barden[4], Catherine A. Pilachowski[5], Constantine P. Deliyannis[5], Dianne Harmer[6], Robert Mathieu[7], Søren Meibom[8], Søren Frandsen[9], and Jerome A. Orosz[1]
[1] San Diego State University, Department of Astronomy, San Diego, CA 92182, USA; esandquist@sdsu.edu
[2] University of California, Santa Cruz, UCO/Lick Observatory, 1156 High Street, Santa Cruz, CA 95064, USA
[3] University of Texas, McDonald Observatory, HC75 Box 1337-L, Fort Davis, TX 79734, USA
[4] Leibniz-Institut für Astrophysik Potsdam, An der Sternwarte 16, D-14482 Potsdam, Germany
[5] Department of Astronomy, Indiana University, Bloomington, IN 47405, USA
[6] National Optical Astronomy Observatory, 950 N. Cherry Avenue, Tucson, AZ 85719, USA
[7] Department of Astronomy, University of Wisconsin–Madison, 475 North Charter Street, Madison, WI 53706, USA
[8] Harvard–Smithsonian Center for Astrophysics, Cambridge, MA 02138, USA
[9] Stellar Astrophysics Centre, Department of Physics and Astronomy, Aarhus University, Ny Munkegade 120, DK-8000 Aarhus C, Denmark
Received 2022 August 28; revised 2022 October 14; accepted 2022 October 19; published 2022 December 6

Abstract

We present analyses of improved photometric and spectroscopic observations for two detached eclipsing binaries at the turnoff of the open cluster NGC 752: the 1.01 days binary DS And and the 15.53 days BD +37 410. For DS And, we find $M_1 = 1.692 \pm 0.004 \pm 0.010 M_\odot$, $R_1 = 2.185 \pm 0.004 \pm 0.008 R_\odot$, $M_2 = 1.184 \pm 0.001 \pm 0.003 M_\odot$, and $R_2 = 1.200 \pm 0.003 \pm 0.005 R_\odot$. We either confirm or newly identify unusual characteristics of both stars in the binary: the primary star is found to be slightly hotter than the main-sequence turnoff and there is a more substantial discrepancy in its luminosity compared to models (model luminosities are too large by about 40%), while the secondary star is oversized and cooler compared to other main-sequence stars in the same cluster. The evidence points to nonstandard evolution for both stars, but most plausible paths cannot explain the low luminosity of the primary star. BD +37 410 only has one eclipse per cycle, but extensive spectroscopic observations and the Transiting Exoplanet Survey Satellite light curve constrain the stellar masses well: $M_1 = 1.717 \pm 0.011 M_\odot$ and $M_2 = 1.175 \pm 0.005 M_\odot$. The radius of the main-sequence primary star near $2.9 R_\odot$ definitively requires large convective core overshooting (>0.2 pressure scale heights) in models for its mass, and multiple lines of evidence point toward an age of $1.61 \pm 0.03 \pm 0.05$ Gyr (statistical and systematic uncertainties). Because NGC 752 is currently undergoing the transition from nondegenerate to degenerate He ignition of its red clump stars, BD +37 410 A directly constrains the star mass where this transition occurs.

Unified Astronomy Thesaurus concepts: Eclipsing binary stars (444); Spectroscopic binary stars (1557); Open star clusters (1160); Low mass stars (2050); Stellar ages (1581); Stellar physics (1621)

Supporting material: machine-readable tables

1. Introduction

Open star clusters have long been testing grounds for models of how stars change with age. However, a critical missing piece of information has been precisely measured star masses. Stellar ages must always be measured via models, and without mass information we are at the mercy of systematic errors resulting from inaccuracies in the physics and chemical composition we encode in the models. This study is part of a larger project to measure precise masses (as well as other characteristics) for stars in open clusters in order to identify these issues, and improve our models of stars and measurements of age.

The star cluster NGC 752 is a relatively nearby and moderately old object. Notable previous estimates of NGC 752's age range from 1.34 Gyr (Agüeros et al. 2018) to 1.58 Gyr (Bartašiūtė et al. 2007), and have generally been based on analysis of color–magnitude diagram (CMD) information for member stars in various filter combinations. While the uncertainties in quoted ages are typically 40–60 Myr, the uncertainties are undoubtedly underestimates because they do not include systematic errors involving correlated errors in distance, reddening, and color–$T_{\rm eff}$ relations, as well as uncertainties in the physics used in the stellar models. New data, such as stellar masses and precise distances, will help eliminate these issues.

NGC 752 is an interesting target for stellar astrophysics in a few other ways. The cluster appears to be old enough that its brightest main-sequence stars, including those at the turnoff, just miss the red edge of the instability strip for δ Sct pulsating stars. Breger (1969) found no pulsators in one of the only studies of short-period variability in the cluster. One γ Dor star is known (PLA 455; Smalley et al. 2011), and because γ Dor pulsation is generally found on the faint, red side of the δ Sct instability strip, this supports the idea that the cluster's turnoff is just redward of the edge. The cluster's age puts it in an interesting range for constraining the spindown of single main-sequence stars, and it may be useful for calibrating gyrochronology (Barnes 2007). Agüeros et al. (2018) presented a first study of the rotation periods of NGC 752 stars, although they presented results on a relatively small number of stars well below the turnoff in the K and M spectral types. Based on the magnitude extent of its red clump, NGC 752 appears to contain

* Based on observations made with with the Hobby–Eberly Telescope, which is a joint project of the University of Texas at Austin, the Pennsylvania State University, Stanford University, Ludwig-Maximilians-Universität München, and Georg-August-Universität Göttingen.

Original content from this work may be used under the terms of the Creative Commons Attribution 4.0 licence. Any further distribution of this work must maintain attribution to the author(s) and the title of the work, journal citation and DOI.

two different kinds of core He burning stars: ones that ignited He burning in nondegenerate gas, and ones that had a degenerate flash ignition (Girardi et al. 2000). Measurement of the masses of evolved stars in the cluster and the cluster age would constrain this important transition in stars.

For precision measurements of stellar masses, binary systems are unmatched. For example, Torres et al. (2010) tabulate systems with masses and radii measured to better than ±3% uncertainty. As luck would have it, there are at least two eclipsing binaries at or near the turnoff of NGC 752 that can provide masses for astrophysical inquiries in the cluster. The short-period detached eclipsing binary DS And has been known since the observations of Alksnis (1961), with major studies of the binary by Schiller & Milone (1988) and Milone et al. (2019). From the standpoint of stellar physics, the two stars in this binary are interesting because they fall in a range ($\sim$1.2–2.0$M_{\odot}$) in which a convective core is springing up and increasing in size as mass increases due to increasing core temperature and stronger CNO cycle nuclear energy release. Ad hoc algorithms for convective core overshooting have been introduced to explain unexpected characteristics of the stars. The issue is strongly linked to age because the extent of the mixed core affects the amount of fuel available for hydrogen burning on the main sequence. Without a proper accounting of how the convective core develops as a function of mass, we should expect there to be systematic error in derived ages.

Despite the short span since the last study by Milone et al. (2019), we present a new analysis of DS And, and show that we have significantly improved the precision of measurements of the stars in the binary. We describe extensive new time-series photometry of the binary along with new high signal-to-noise ratio spectroscopy and improved analysis of previous spectroscopy, utilize the vast amount of photometry on the cluster to discuss spectral energy distributions for the binary's stars, and present new modeling to derive the characteristics of the orbits and of the stars themselves.

BD +37 410 was identified as a double-lined spectroscopic binary by Daniel et al. (1994), and as an eclipsing binary by Pribulla et al. (2009). It is a brighter system than DS And, which probably identifies it as having a more evolved primary star. The binary period (15.534 days) is long enough that the two stars have probably evolved independently of each other, without enough tidal interaction to circularize the orbit (Meibom & Mathieu 2005). Radial velocities were published by Pribulla et al. (2010) and Mermilliod et al. (2009), and a spectroscopic orbital solution was derived by Pribulla et al. (2010). However, because the system only shows one eclipse per orbital cycle, it has not been studied in detail, as it is unlikely to provide reliably measured radii for the two stars. Despite this, the masses of the stars can be measured, and can provide additional limits on the cluster age because the primary star resides near the very tip of the main sequence.

2. Cluster Properties

Before discussing the observation and analysis of the binaries, we briefly summarize cluster information that will be needed for a proper discussion of age indicators.

2.1. Chemical Composition

Knowledge of the chemical composition of cluster stars will affect our interpretation of the characteristics of the binary stars. For that reason, we summarize spectroscopic abundance studies of NGC 752 stars in Table 1 and briefly discuss the cluster's composition.

Table 1
Spectroscopic Abundance Measurements of NGC 752 Stars

		N		References
[Fe/H]	0.00 ± 0.06	10	RGB	1
[Fe/H]	-0.01 ± 0.06	23,6	RGB,MS	2
[M/H]	-0.032 ± 0.037	36	MS	3
[Fe/H]	-0.02 ± 0.05	10	RGB	4
[Fe/H]	-0.063 ± 0.014	33	solar-type MS	5
$[Fe/H]_{I}$	-0.04 ± 0.03	4	RGB	6
$[Fe/H]_{II}$	-0.02 ± 0.02	4	RGB	6
[Fe/H]	$+0.08 \pm 0.04$	4	RGB	7
[Fe/H]	$+0.013 \pm 0.009$	7	MS	8
[Fe/H]	-0.102 ± 0.022	8	MS	9

References. (1) Böcek Topcu et al. (2020), (2) Lum & Boesgaard (2019), (3) Guo et al. (2017), (4) Böcek Topcu et al. (2015), (5) Maderak et al. (2013), (6) Reddy et al. (2012), (7) Carrera & Pancino (2011), (8) Sestito et al. (2004), Taylor (2007), (9) Hobbs & Thorburn (1992), Taylor (2007).

An important part of examining the literature abundances is to ensure that the abundance scale is correct relative to the Sun. Lum & Boesgaard (2019) set the $\log gf$ values for their lines based on measurements of a solar reference spectrum taken at the National Solar Observatory (Wallace et al. 2011) after comparing to Asplund et al. (2009, A09) abundances, and determined NGC 752 star Fe abundances relative to the same A09 abundances. Guo et al. (2017) examined the composition of twilight spectra, and found $[M/H]_{\odot} = 0.004 \pm 0.015$. Böcek Topcu et al. (2015) ran their abundance analysis on the Kurucz et al. (1984) integrated solar flux atlas to derive solar Fe abundance. Maderak et al. (2013) used a solar spectrum with the abundance analysis tuned to return a target A(Fe) value for it. Reddy et al. (2012) determined solar abundance of Fe using an ATLAS9 model solar spectrum. Carrera & Pancino (2011) conducted an abundance analysis of an ESO solar spectrum of Ganymede. Sestito et al. (2004) used a solar spectrum from the Moon and adjusted their oscillator strengths to produce $\log n(\mathrm{Fe})_{\odot} = 7.52$. Hobbs & Thorburn (1992) also adjusted their oscillator strengths to produce a solar iron abundance for solar equivalent widths.

From the most recent spectroscopic measurements, there seems to be some agreement that NGC 752 stars have solar or slightly subsolar iron abundances—straight or weighted averages of the values in Table 1 give [Fe/H] = −0.02. For the most part, we will assume [Fe/H] = 0 for NGC 752 stars. There does not appear to be evidence of a systematic difference between RGB and MS stars, as might be expected if diffusion played a role in modifying surface abundances.

Comparisons with stellar models require that the abundances relative to the Sun be translated into a heavy element mass fraction Z. This in turn requires us to know the solar value, but this is still significantly uncertain itself. Recent values range from $Z_{\odot} = 0.0122$ (Asplund et al. 2005) to 0.0153 (Caffau et al. 2011), with 0.0139 ± 0.0006 a recent re-evaluation by Asplund et al. (2021). Most recently, Magg et al. (2022) extensively re-evaluated many aspects of solar abundance determinations and arrived at $Z = 0.0177$, showing that the higher metal abundance brings solar models into greater agreement with helioseismology constraints. The isochrone models we will use most

frequently in comparisons below will use $Z = Z_{\odot} = 0.0152$, but we will look at consequences of other possible metallicities.

2.2. Reddening and Distance

Taylor (2007) critically examined measurements of the cluster's reddening, and settled on $E(B-V) = 0.044 \pm 0.0034$. Twarog et al. (2015) used Strömgren *uvby*CaHβ photometry to derive $E(B-V) = 0.034 \pm 0.004$. Although these values disagree somewhat, the reddening seems to be quite small, and should not be a major uncertainty in the analysis of cluster CMDs. We will generally use the larger Taylor value below.

The weighted average parallax for NGC 752 members in Gaia Data Release 2 (DR2) has been determined as 2.2304 ± 0.0027 mas (Gaia Collaboration et al. 2018), or 2.239 ± 0.005 mas (Cantat-Gaudin et al. 2018). However, there are a number of studies indicating that Gaia parallaxes are systematically offset to smaller values (and implying that objects are systematically closer than Gaia indicates; Lindegren et al. 2018; Schönrich et al. 2019; Zinn et al. 2019). Bailer-Jones et al. (2021) determined distances of $431.7^{+3.8}_{-3.2}$ pc for DS And and $434.1^{+19.6}_{-18.5}$ pc for BD +37 410 from Gaia Early Data Release 3 (EDR3) data. The quoted uncertainties include consideration of uncertainties in the zero-point of the Gaia parallax scale. The corresponding distance moduli [$(m-M)_0 = 8.176^{+0.019}_{-0.016}$ and $8.19^{+0.11}_{-0.09}$] are in excellent agreement with cluster determinations by Agüeros et al. (2018) and Twarog et al. (2015): $8.21^{+0.04}_{-0.03}$ and 8.20 ± 0.05 (or around 436.5 and 438.5 pc), respectively.

These estimates are, however, very different than the distance determined by Milone et al. (2019) as part of their binary star modeling of DS And: $(m-M)_0 = 8.390 \pm 0.018 \pm 0.060$, or $477 \pm 4 \pm 12$ pc. About half of the discrepancy appears to be due to their allowance for a third light source in the system.

2.3. Cluster Membership, Single Stars, and Spectral Energy Distributions

Clear identification of NGC 752 stars is important for understanding the properties of the stars of DS And in context, and for constraining physics that affects the evolution of the stars at the cluster turnoff. The most comprehensive membership studies of the cluster have been Platais (1991), Daniel et al. (1994), Agüeros et al. (2018), and Cantat-Gaudin et al. (2018). The last of these was the first application of Gaia Data Release 2 to the cluster as a whole, and is the source of proper-motion and parallax cuts we use here. We also used radial-velocity information from Daniel et al. (1994) and Agüeros et al. (2018) to identify binary stars and remove them from consideration as representatives of single stars. After these cuts, we attempted to eliminate photometric binaries using color–magnitude diagrams using the most precise photometry. Unresolved binary systems containing main-sequence stars are found in a band brighter and redder than the sequence of single stars. We primarily used the Gaia Early Data Release 3 (EDR3) diagram in ($G_{BP} - G_{RP}$, G), a Strömgren ($b-y$, y) diagram (Twarog et al. 2015), and a Vilnius ($Y-V$, V) diagram (Zdanavičius et al. 2010), as shown in Figure 1.

Thanks to its small distance, NGC 752 stars have high signal-to-noise ratio photometric observations in many wavelength bands from deep in the ultraviolet to deep in the infrared. These data can be used to generate well-sampled spectral energy distributions (SEDs), and fit for effective temperature $T_{\rm eff}$ and bolometric flux $F_{\rm bol}$. In combination with Gaia distance measurements, it is possible to put many stars in the Hertzsprung–Russell (HR) diagram reliably. The sources for the photometry we used are given in Appendix, along with some notes on the data sets and conversion to fluxes.

3. Observations and Data Reduction

3.1. Time-series Photometry

We made primary use of photometry from the Transiting Exoplanet Survey Satellite (TESS; Ricker et al. 2015) taken in sector 18 of the northern hemisphere campaign. DS And was not a target observed at two-minute cadence, but TESS records full-frame images (FFIs) every 30 minutes, and we derived a light curve from the FFIs using the software `eleanor` (Feinstein et al. 2019). The TESS observations cover a period of almost 25 days, with a data gap of about 3 days roughly in the middle. In addition, the initial 2.5 days of the observations showed variations that could not be corrected and appeared to be affected by instrumental systematics, so we did not include those data in the analysis. DS And is a fairly bright and isolated target, and so we used a simple circular aperture of 2.5 pixel radius for the photometry. We found that the `eleanor` light curves that used corrections from the built-in cotrending analysis (removing trends shared with nearby stars on the frames) showed poorer consistency from cycle to cycle, so we used the light curve based on raw fluxes.

We also used TESS photometry for BD +37 410. Two eclipses were observed during the campaign, although one was observed in the initial days when the data quality was poorer. Using the Quick Look Pipeline (QLP) light curve (Huang et al. 2020), the systematics were corrected well enough that we decided to include that eclipse in the light-curve analysis. For the later analysis, we also included photometry taken around the time of the noneclipsing conjunction.

Our ground-based photometric observations of DS And were taken with the 1 m telescope at Mount Laguna Observatory with the CCD 2005 camera. This camera uses a 2048 × 2048 CCD with a field of view approximately 13′.5 on a side. Observations were taken during the course of one season in 2010 with the intention of fully covering eclipse phases in BVR_CI_C filters, along with sparser coverage of out-of-eclipse phases. The nights of observation are given in Table 2.

We took additional observations at the 1 m telescope in U during 2020 in order to constrain the spectral energy distribution for the component stars. These observations utilized a newer camera (called UltraCam) with a similar field of view but lower read noise.

The images were processed in IRAF[10] with standard techniques to subtract the overscan region for each image and a master bias image, and divide out a normalized master flat field. A somewhat nonstandard step was correction for a nonlinearity in the CCD response during the 2010 observations that resulted from improperly set readout amplifier voltages. The correction (D. Leonard 2016, private communication) used was

$$\mathrm{ADU_{cor}} = \mathrm{ADU} \times [1.01353 - 0.11576 \times (\mathrm{ADU}/32767) + 0.0296378 \times (\mathrm{ADU}/32767)^2].$$

[10] IRAF is distributed by the National Optical Astronomy Observatory, which is operated by the Association of Universities for Research in Astronomy (AURA) under a cooperative agreement with the National Science Foundation.

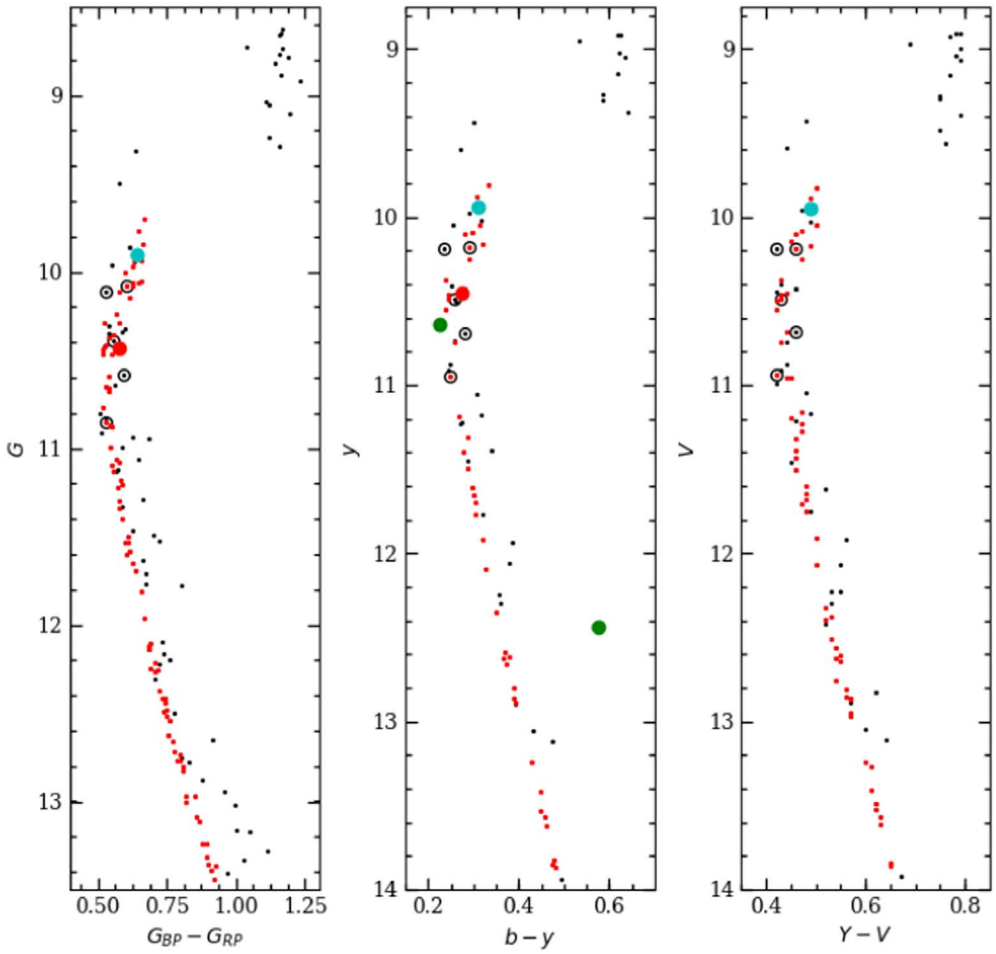

Figure 1. Precise CMDs used for selecting likely single-star members of the NGC 752 cluster, with Gaia EDR3, Strömgren (Twarog et al. 2015), and Vilnius (Zdanavičius et al. 2010) photometry shown from left to right. Gaia-selected likely binary members are shown in black, with photometrically selected single-star members in red. Open circles show known chemically peculiar stars (Garrison 1972). Photometry of BD +37 410 is shown with the cyan point, the DS And system at quadrature is the larger red point, and the positions of the DS And primary and secondary stars (as inferred from light curves) are shown with green points.

This was applied to flat field and cluster images using the procedure `irlincor` before the master flat field image was created and applied to the cluster images. The corrections significantly improved the consistency of light curves that were taken under differing airmass and atmospheric conditions because we generally adjusted exposure times to maintain high photon counts for DS And.

Aperture photometry was conducted using the `DAOPHOT` package within IRAF. We employed 12 apertures to photometer all stars on each frame, and subsequently constructed a curve of growth using the routine `mkapfile`. The curve of growth was used to correct magnitudes measured in the aperture with the highest signal-to-noise ratio to that of a common large radius. We then used an ensemble photometry technique (Honeycutt 1992; Sandquist et al. 2003) to adjust the zero-points for each image in order to minimize the median magnitude difference for stars from observation to observation. This improves the fidelity of the differential photometry, but we saw clear evidence of changes in the brightness of DS And on some nights. We corrected for these variations by applying nightly shifts. The biggest need for these corrections was in R_C band, including +0.04 mag to 2010 September 17, −0.03 mag to 2010 October 23, +0.025 mag to 2010 December 2, and +0.03 mag to 2010 December 9. Smaller shifts were applied to a few nights in B, but corrections did not appear to be needed for V and I_C bands.

We incorporated V photometry from two other sources in order to extend the time baseline of eclipse observations. Breger (1968) presented 51 photoelectric observations from five nights in 1967, providing complete coverage of the primary eclipse. Breger (1968) quotes a standard error of less than 0.01 mag for their differential photometry relative to a comparison star. We also employed data from the Northern Sky Variability Survey (NSVS; Woźniak et al. 2004). Although the NSVS data typically were limited to a few observations during a night spaced by a few days, the long-term observations produced a well-sampled light curve. In total there were 288 observations from NSVS over the course of 225 days between HJD 2,451,397 (1999 December 6) and 2,451,623 (2000 March 19).

We also considered the $UBVR_CI_C$ photoelectric photometry data set discussed in detail by Milone et al. (2019). These data were taken in the 1982–1983 observing season. Observations in BVR_CI_C filters were taken on a 41 cm telescope at the University of Calgary's Rothney Astrophysical Observatory, and in all five filters at the 90 cm telescope at McDonald Observatory and at the 60 cm telescope at Table Mountain Observatory. We initially assigned different but uniform uncertainties to observations taken in the same filter at the

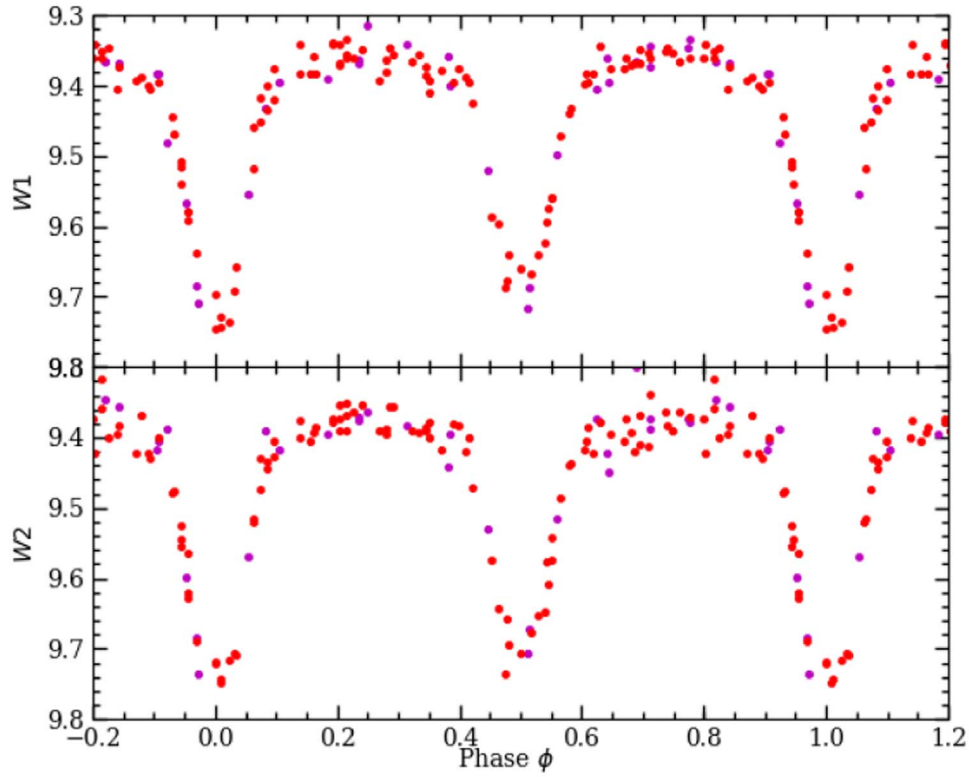

Figure 2. DS And W1 and W2 light curves from WISE (magenta points) and NEOWISE-R (red) photometry (Chen et al. 2018).

Table 2
Photometry Observations at the Mount Laguna 1 m Telescope

UT Date	Filters	mJD Start[a]	N_{obs}
2010 Aug 31	R_CI_C	55,441.0273	79
2010 Sep 1	BV	55,441.9295	80
2010 Sep 7	B	55,446.7323	274
2010 Sep 8	R	55,447.7294	390
2010 Sep 11	V	55,450.7273	325
2010 Sep 12	I_C	55,451.7193	465
2010 Sep 17	VR_CI_C	55,457.9116	138
2010 Oct 11	V	55,480.9278	10
2010 Oct 14	V	55,483.6378	353
2010 Oct 16	V	55,485.9787	194
2010 Oct 17	I_C	55,486.6284	658
2010 Oct 23	BR_C	55,492.6349	177
2010 Oct 24	BR_C	55,493.6398	309
2010 Oct 26	BR_C	55,495.8442	156
2010 Nov 5	BVI_C	55,505.5874	395
2010 Nov 17	VR_CI_C	55,517.9113	40
2010 Nov 30	B	55,530.7061	304
2010 Dec 2	V	55,532.5626	352
2010 Dec 4	R_C	55,534.5901	387
2010 Dec 9	BR_C	55,539.5825	190
2020 Jul 7	U	59,037.8834	60
2020 Jul 24	U	59,055.8443	64
2020 Aug 10	U	59,072.7945	87
2020 Sep 4	U	59,097.7292	120

Note.
[a] mJD = BJD − 2,400,000.

same facility, but we adjusted these uncertainties to be statistically consistent with the rms scatter around best-fit models. It is with these kinds of adjustments that we weight the quality of different photometric data sets relative to each other.

Table 3
Time-series Photometry Used in Modeling DS And

mJD[a]	Filter	mag.	σ
59,037.884249	U	11.8810	0.0222
59,037.889944	U	11.8581	0.0180
59,037.892097	U	11.8472	0.0150
59,037.893509	U	11.8592	0.0174
59,037.895905	U	11.8546	0.0108
59,037.898417	U	11.8462	0.0117
59,037.900616	U	11.8447	0.0096

Note.
[a] mJD = BJD − 2,400,000.

(This table is available in its entirety in machine-readable form.)

Finally, we used light curves from the Wide Field Infrared Explorer (WISE; Wright et al. 2010) in the W1 and W2 bandpasses provided by Chen et al. (2018). These are depicted in Figure 2.

The complete photometric data set is given in Table 3.

3.2. Spectral Energy Distributions (SEDs)

Because of the vast amount of photometry available for NGC 752 stars, photometric SEDs can be of use in deriving characteristics of single cluster stars, as well as components of the eclipsing binaries. The Appendix discusses the photometry we have assembled for NGC 752 cluster members from the ultraviolet to deep in the infrared, as well as details of our procedure for fitting the SEDs. After selecting cluster member stars from Gaia parallax and proper-motion information, we rejected spectroscopic binaries that have been previously identified in the literature (and tabulated by Agüeros et al. 2018).

We then identified likely single main-sequence stars that were consistently near the blue edge of the main-sequence band in CMDs with precise photometry—stars more than about 0.03 mag from the blue edge of the main sequence in the Gaia ($G_{BP} - G_{RP}$, G) CMD were also rejected as likely binaries.

For BD +37 410, the luminosity ratio for the stars appears to be small ($L_2/L_1 = 0.11$; Pribulla et al. 2010), and so a fit places a lower limit on the effective temperature of the brighter primary star. For the DS And system, the brightness is continually varying, although with relatively small variations (~0.06 mag) outside of the eclipses. The eclipses cover approximately one-third of an orbital cycle. Because the majority of literature photometric measurements of DS And were probably not taken at phases that would give a measure of the average brightness, significant scatter will be introduced by the binary's variability even if all of the measurements were taken out of eclipse. We have corrected for this in wavelength bands where we have light-curve information, as described below.

3.2.1. Photometric Deconvolution and Effective Temperatures of DS And

Calibrated photometry of the DS And binary can in principle give us constraints on the characteristics of the component stars, but this is complicated by the continuous photometric variation due to the eclipses and ellipsoidal variations due to the nonspherical shapes of the stars. Measurements of the system at the orbital quadratures represent the total brightness of the system best because we see the maximal area of both stars. With well-sampled measurements during the secondary eclipse, we observe the complete blocking of the flux contribution of the secondary star when the stars are end-on. This provides a direct measurement of the brightness of the secondary star, and the brightness during secondary eclipse also provides a solid lower limit to the flux from the primary star. With a correction for the ellipsoidal shape, we can recover the flux from the primary star. Colors measured during the secondary eclipse should be the colors of the primary star.

Milone et al. (2019) raise the possibility of third light flux contributions from an additional star that is blended with those from the binary, whether due to a bound member of the system or an unassociated star. Calculations of the secondary star's photometry are unaffected by any third light, but if present, it would remain after the secondary star's light is subtracted from the system photometry. Regardless, precise determination of the CMD positions of the secondary star and the system with the secondary star's light subtracted (relative to other stars in the cluster) could help identify potential third light effects or other abnormalities due to the close interaction of the stars in the eclipsing binary. The photometric characteristics of the system (best-fit maximum brightness and secondary eclipse depth, as well as luminosity ratios) are given in Table 4, and details of the calculations are given below.

We first assembled well-sampled light curves from available sources and modeled each individually in order to establish the maximum brightness of the system and measure the luminosity ratio (secondary divided by total) in each band. We utilized $UBVR_CI_C$ light curves from our observations and those of Schiller & Milone (1988), as well as the NSVS V-band light curve.

The TESS light curve provides a measure of the relative brightness of the two stars in a relatively broad bandpass centered near the I_C filter. The filter for TESS is similar to the RP filter for Gaia, and can provide guidance on decomposing the Gaia photometry of the two stars in DS And. We also extracted a light curve from the SuperWASP Data Release 1 database (Butters et al. 2010), in part because the SuperWASP filter (covering around 400–700 nm) is similar to the Gaia BP filter. Because of systematics visible in the SuperWASP light curves, we restricted ourselves to data from just one of the cameras (ID number 141) and calculated variations differentially relative to another nearby bright star (NGC 752 165). The light curve containing 3155 observations taken between 2007 August 20 and December 17, and a model fit are shown in Figure 3.

Finally, we utilized light curves in the WISE W1 and W2 bandpasses (Chen et al. 2018) in order to get information on the system in the far-infrared.

In cases where there are fewer observations at known times, the magnitude measurements still contain information about the system flux within the filter bandpass. With the well-determined ephemeris (such as a period uncertainty of 2.0×10^{-8} days), fits to the observations allow us to estimate the total system flux (measurable at the orbit quadratures) and the primary star contribution using secondary star eclipse depths in similar bandpasses. Twarog et al. (2015) obtained limited time-series observations of DS And in Strömgren *uvby* filters, typically 24 observations in each filter mostly in the primary eclipse. These were provided by B. Twarog (2022, private communication).

The 2MASS infrared survey observed DS And at a single time (JD 2,451,127.7755), which was reasonably close to one of the quadratures at phase 0.38. Because we have

Table 4
DS And Light-curve Characteristics

Filter	m_{max}	Δm_λ[a]	$(L_2/L_{tot})_\lambda$	References
FUV	18.394 ± 0.014			
NUV	14.254 ± 0.011			
u	12.153 ± 0.006		0.125	1
U	10.852 ± 0.005		0.077	2
U		0.247	0.121	3
v	11.126 ± 0.006		0.124	1
B	10.833 ± 0.009	0.255	0.107	2
B		0.251	0.125	3
b	10.726 ± 0.007		0.145	1
V	10.439 ± 0.004	0.275	0.138	2
V		0.265	0.148	3
V		0.281	0.158	4
y	10.451 ± 0.008		0.161	1
SuperWASP	10.60	0.288	0.162	5
R_C	10.222 ± 0.005	0.270	0.146	2
R_C		0.300	0.167	3
I_C	9.959 ± 0.012	0.276	0.159	2
I_C		0.287	0.172	3
TESS		0.2885	0.174	
J	9.611		0.194	
H	9.441		0.211	
K_s	9.368		0.213	
W1	9.352	0.310	0.210	6
W2	9.368	0.314	0.208	6
W3	9.21			

Note.
[a] Magnitude difference between brightness maximums at phase $\phi = 0.25$ and 0.75, and the brightness minimum in the secondary eclipse ($\phi = 0.5$).
References. (1) Twarog et al. (2015), (2) Milone et al. (2019), (3) This paper, (4) NSVS; Woźniak et al. (2004), (5) Butters et al. (2010), (6) Chen et al. (2018).

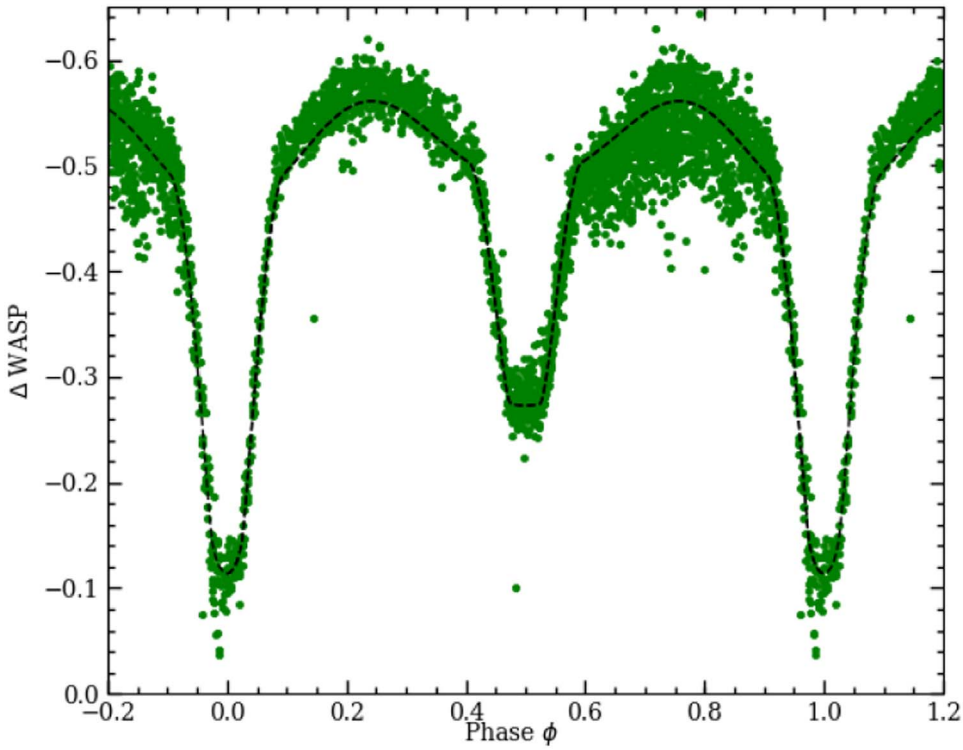

Figure 3. DS And light curve from SuperWASP camera 141, computed differentially relative to nearby star NGC 752 165.

well-sampled light curves at wavelengths on either side of the 2MASS bands, we can make informed estimates of what the maximum magnitudes and luminosity ratios are.

The Galaxy Evolution Explorer (GALEX) observed DS And in the FUV passband at a phase close to the quadrature ($\phi = 0.70$), and so we take this as being the system magnitude. The contribution from the cooler secondary star is inferred to be less than 10% in this wavelength range.

Using fitted light curves, we can identify where the primary star (plus possible third star) would be in some CMDs. The color during secondary eclipse should be representative of the color of the primary star, and the flux during secondary eclipse should be a lower limit to the flux of the primary star, only off by a few percent due to ellipsoidal variations. We correct for the ellipsoidal variation in each band using our best-fit models (see Section 4.2).

We have fitted the SED of DS And A using the algorithm discussed in the Appendix. The primary star was best fit with $T_{\rm eff} = 7070$ K, as shown in Figure 4. We estimate the statistical measurement uncertainty from the range in IRFM values determined from the different 2MASS bands (40 K from minimum to maximum). An uncertainty of 0.01 in $E(B-V)$ results in a shift of approximately 50 K in the measured values, with lower reddening leading to lower measured temperatures. We consider the reddening uncertainty to be statistical here, and add it in quadrature with the measurement uncertainty. We also assign an systematic uncertainty of ± 100 K to account for uncertainties in the model temperature scale. Our final value is 7070 ± 55 (stat.) ± 100 (sys.) K. This compares well with $7056 \pm 21 \pm 140$ K from Milone et al. (2019), found entirely through their modeling of different combinations of $UBVR_CI_C$ light curves.

The fitted bolometric flux at Earth for the primary star comes out to be $F_{\rm bol} = 1.56 \times 10^{-9}$ erg s^{-1} cm^{-2}. Extinction uncertainties contribute at about a 3% level in this measurement, and uncertainties in the ultraviolet (where there is some lack of coverage and a mismatch between models and available measurements, but also a relatively small 5% contribution to the total flux) result in another 1% uncertainty. Together this produces an uncertainty of $\pm 0.05 \times 10^{-9}$ erg s^{-1} cm^{-2}.

With the corrected Gaia distance (see Section 2.2), this produces $L_1 = 9.25 \pm 0.34 L_\odot$. This is in agreement with the Milone et al. (2019) value $9.58 \pm 0.12 \pm 0.20 L_\odot$, with the difference largely because they derived a larger distance modulus.

Comparisons to other NGC 752 stars are important for reliably determining whether the properties of the stars in DS And have been affected by their interactions within the short-period binary. While the $(B-V, V)$ photometry of Daniel et al. (1994) is the only large data set of Johnson–Cousins photometry specifically of the cluster, there are other sources of high signal-to-noise ratio photometry that can be transformed into the Johnson–Cousins system. We used relations from Harmanec & Božić (2001) to convert Strömgren $(b-y)$ and $(u-b)$ colors to $(B-V)$ and $(U-B)$, and Geneva U_G, B_G, and V_G magnitudes to Johnson U, B, and V. We also used a relation from Cousins (1987) to transform Strömgren $(b-y)$ to $(V-I_C)$. For the Vilnius system, we transformed from $(U_V - Y_V)$ to $(U-B)$; (Forbes 1996), and from $(X_V - V_V)$ and $(Y_V - V_V)$ to $(B-V)$; (Straižys 1992). We compared these transformed photometric data to data taken directly in Johnson–Cousins filters (APASS in $B-V$, and Taylor et al. 2008 in $V-I_C$) where possible.

As can be seen in the $(B-V)$ and $(V-I_C)$ CMDs in Figure 5, the primary star appears to have colors consistent with the main-sequence turnoff of the cluster, but it is significantly bluer in $(U-B)$ than stars at the same V magnitude. The bluest main-sequence stars in $(U-B)$ have $V \sim 11.7$, unlike the CMDs using other colors, clearly

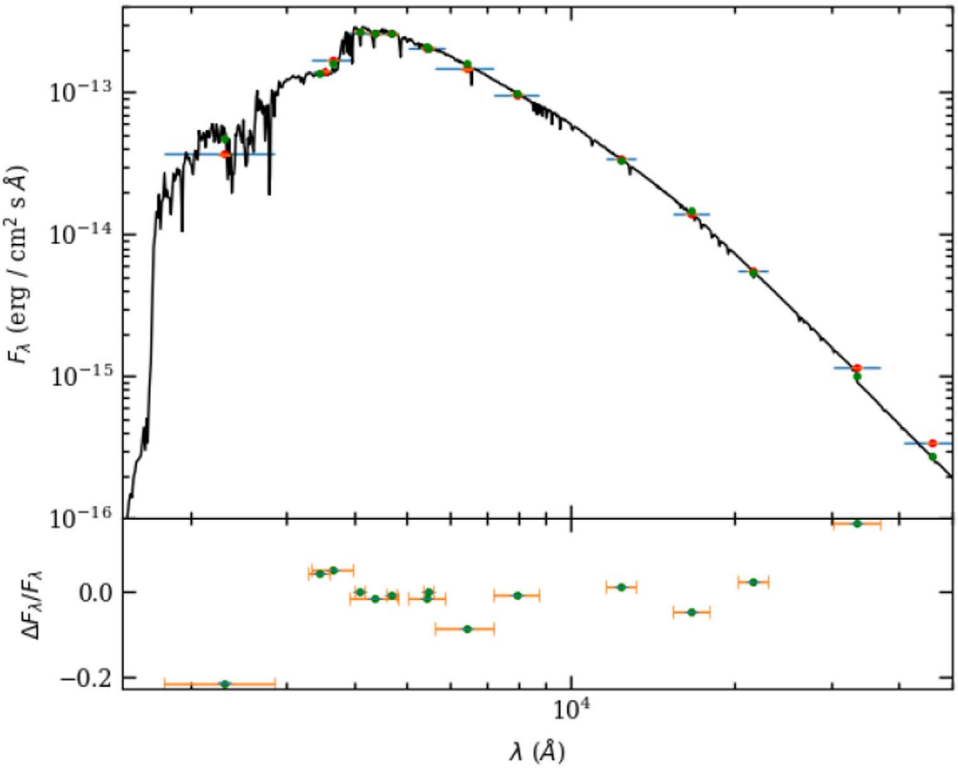

Figure 4. Spectral energy distribution for DS And A as derived from light curves with observations of the secondary star eclipse (red points for photometry). A fitted ATLAS9 model for $T_{\rm eff} = 7070$ K, $\log g = 4.0$, and [Fe/H] = 0 (solid line, and green points for integrations over filter response curves) is shown. Horizontal error bars represent the effective width of the filter. Bottom: fractional difference between the stellar fluxes and the best-fit model fluxes for the ATLAS9 (green) model.

illustrating effects of the Balmer jump on the cluster's turnoff stars. This implies that the primary star has a weaker Balmer jump (more U flux) than expected for similarly bright stars.

Single stars at the cluster turnoff can provide a lower limit to the effective temperature of the primary star. We fitted the photometric SEDs of the two bluest single-star candidates in the Gaia $G_{BP} - G_{RP}$ color (BD+37 417/PLA 477, and TYC 2829-1179-1), and find $T_{\rm eff}$ values of 6955 and 6980 K. The fit for BD+37 417 is shown in Figure 6. These two stars form a conservative bracket in brightness above and below DS And A. The fitted bolometric fluxes were 1.69 and 1.25×10^{-9} erg cm^{-2} s^{-1}, which gives luminosities of $10.0L_\odot$ and $7.42L_\odot$ using the Gaia distance. The luminosities do indeed bracket the value for DS And A, and these $T_{\rm eff}$ measurements are lower limits to that of DS And A if there is no third light for DS And, and if interactions in the binary have resulted in minor changes in surface temperature.

3.2.2. The Secondary Star of DS And

The secondary star is consistently redder or brighter than the locus of single main-sequence stars. This fact is based on the light lost during the total eclipse of the secondary, and is a robust result of the light-curve analysis, but these characteristics are hard to explain. The secondary is very unlikely to have evolved enough in size through single-star nuclear evolution to reach this CMD position during the age of the cluster. Light-curve analysis below implies that the star is not likely to be different from spherical by more than a few percent, and the spectral analysis confirms that the star is rotating at or close to synchronism with the orbit. Short-period binaries with solar-type stars frequently show evidence of inflation of radius, and this has been attributed to inhibition of convection in stars with relatively deep surface convection zones (Torres et al. 2006; Clausen et al. 2009). However, the secondary star of DS And is massive enough that its surface convection zone is likely to contain little of the star's mass. In the 2.18 days binary FL Lyr, the $0.96M_\odot$ secondary star shows much clearer signs of radius inflation than the primary, which is similar in mass to DS And B ($1.22M_\odot$ versus $1.18M_\odot$). In that case though, there is no prior information about the binary's age, and so the primary star could be mildly inflated or simply evolved, as its radius is larger than expected for young main-sequence stars. With a system of known age such as stars in this cluster, it should be possible to distinguish between these scenarios.

An examination of the CMDs in Figure 5 implies that the color deviations between DS And B and the main sequence are greater in shorter-wavelength filters. This is borne out in comparisons with stars at the same V magnitude level, where the largest differences are in the ultraviolet. PLA 255 is a good star for comparison, and a fit to its SED returns $T_{\rm eff} = 6290$ K and $F_{\rm bol} = 2.88 \times 10^{-10}$ erg cm^{-2} s^{-1} (see Figure 7). A similar fit to the 14 filter bands for which we can reconstruct the flux of DS And B returns $T_{\rm eff} = 6100 \pm 43 \pm 100$ K and $F_{\rm bol} = 2.95 \pm 0.07 \times 10^{-10}$ erg cm^{-2} s^{-1} (see Figure 8). Reddening is accounted for in these fits, and contributions to the temperature uncertainty from scatter in the IRFM calculations (±25 K) and reddening uncertainty (±35 K) are included. Using the Gaia distance, we get a luminosity $L_2 = 1.75 \pm 0.05L_\odot$.

Based on these comparisons, the secondary does appear to be significantly lower in surface temperature than cluster main-sequence stars of the same brightness. We will discuss the secondary star in more detail after the binary star analysis.

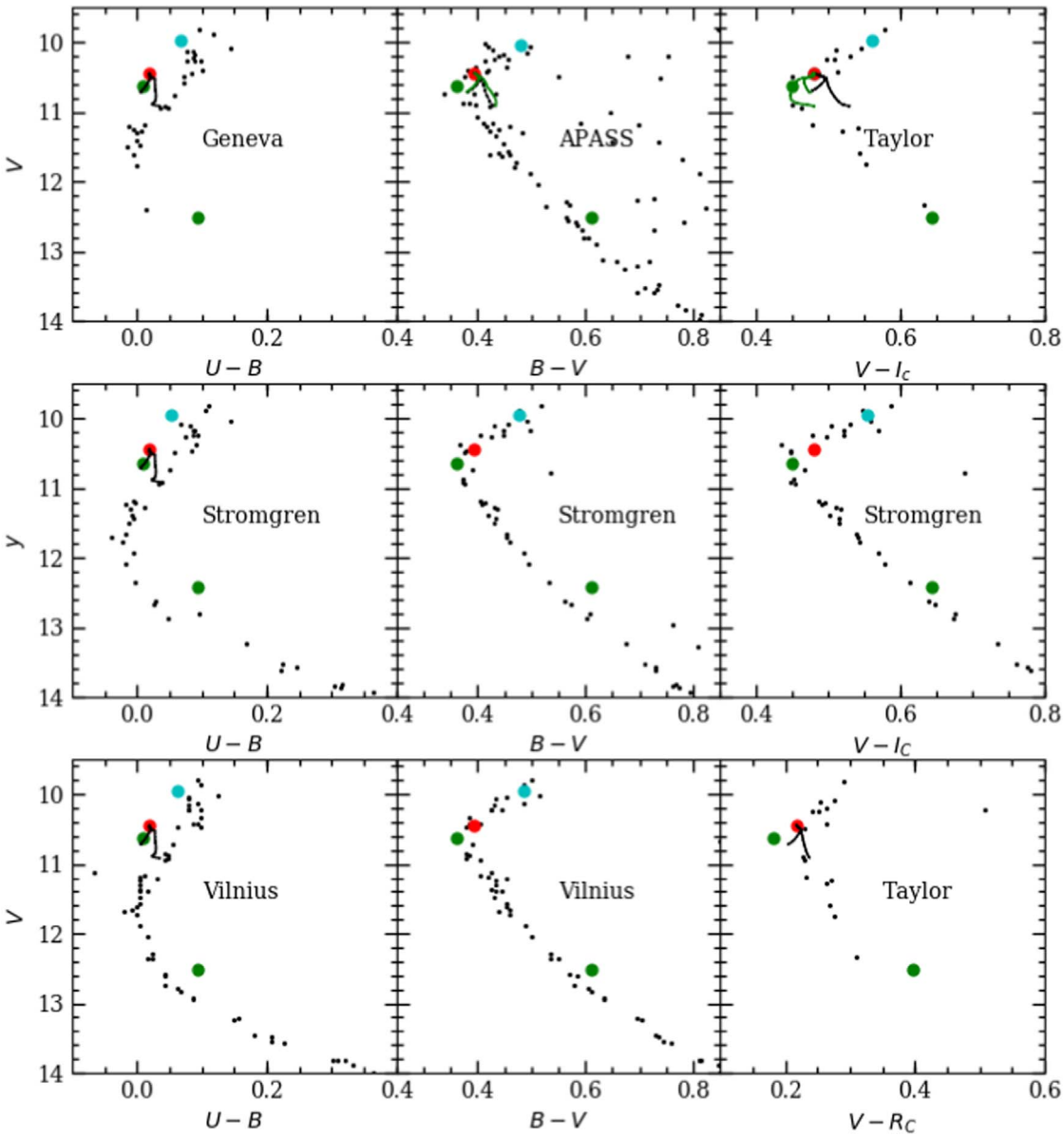

Figure 5. Precise CMDs of likely single-star members of the NGC 752 cluster. Photometry of BD +37 410 is shown with cyan points, the DS And system at quadrature is shown with red points, and the positions of the primary and secondary stars (as inferred from light curves) are shown with green points.

3.2.3. BD +37 410

As seen in Figure 5, BD +37 410 lies comfortably among the most likely single stars brighter than the turnoff in optical and near-infrared CMDs. In the $U-B$ color, it is somewhat bluer than these stars. Regardless, this is one indication that any other bound companions or unassociated blended objects do not contribute greatly to the binary light. The measurement by Pribulla et al. (2010) of an optical luminosity ratio from spectral broadening functions ($L_2/L_1 = 0.11$) localizes the secondary star to $G \approx 12.3$. If the star is a normal main-sequence star of that brightness, it would have nearly the same color as the binary and so a fit to the binary's SED places a lower limit on the effective temperature of the brighter primary star and an upper limit on its luminosity. The fit to the photometric SED with ATLAS9 models returns $T_{\rm eff} = 6480$ K, $\log g \approx 4.0$ (cgs), and $F_{\rm bol} = 3.00 \times 10^{-9}$ erg s^{-1} cm^{-2}. This puts an upper limit on the primary star $L_1 < 15.7 L_\odot$. Our spectroscopy below reveals a more complicated situation than Pribulla et al. understood, and we will discuss this more.

3.3. Spectroscopy

3.3.1. DS And

For DS And, we obtained 17 spectra at the Hobby–Eberly Telescope (HET) with the High Resolution Spectrograph (HRS; Tull 1998) between 2010 August and 2011 September. We used the configuration HRS_30k_central_600g5822_2as_2sky_I-SO_GCO_2x3 for a resolution R = 30,000 on these rapidly rotating stars in all spectra. Exposure times ranged from 1260 to 12,240 s, and we only used the wavelength range 4825–5760 Å from the blue CCD in our subsequent analysis. The data were reduced using the echelle package within IRAF to remove the standard bias and scattered light, extract one-dimensional spectra, and calibrate the wavelength scale. Two observations were taken during morning twilight and had significant solar

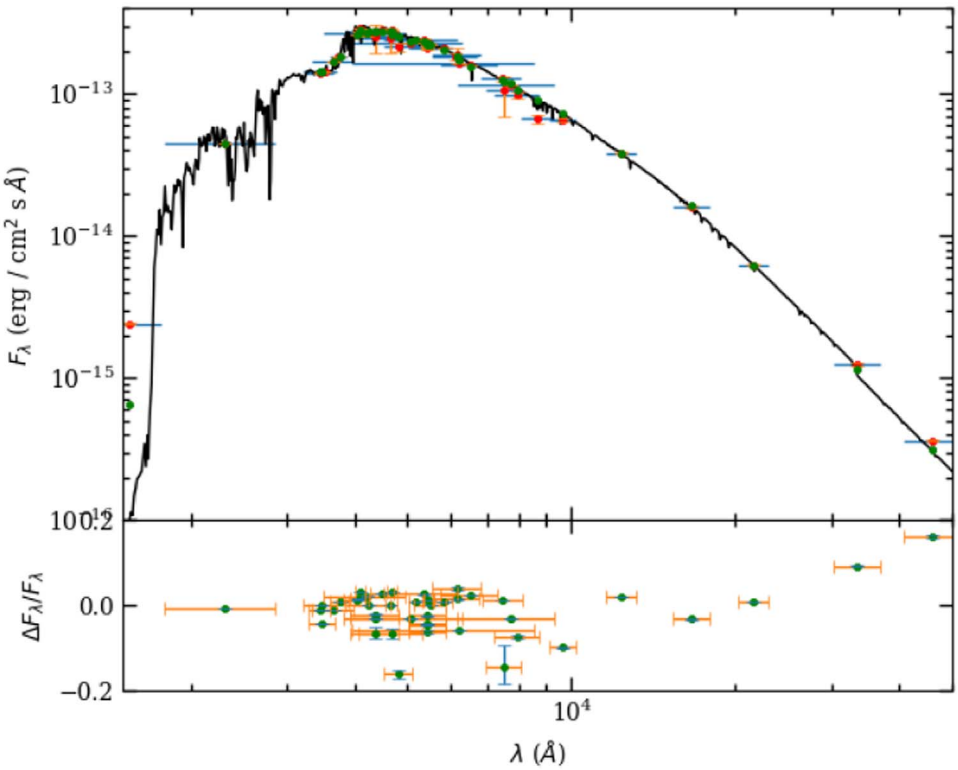

Figure 6. Top: SED for turnoff star BD +37 417 (red points for photometry) and a fitted ATLAS9 model for $T_{\rm eff} = 6955$ K, $\log g = 4.0$, and [Fe/H] = 0 (solid line, and green points for integrations over filter response curves). Bottom: fractional difference between the stellar fluxes and the best-fit model fluxes for the ATLAS9 (green) model.

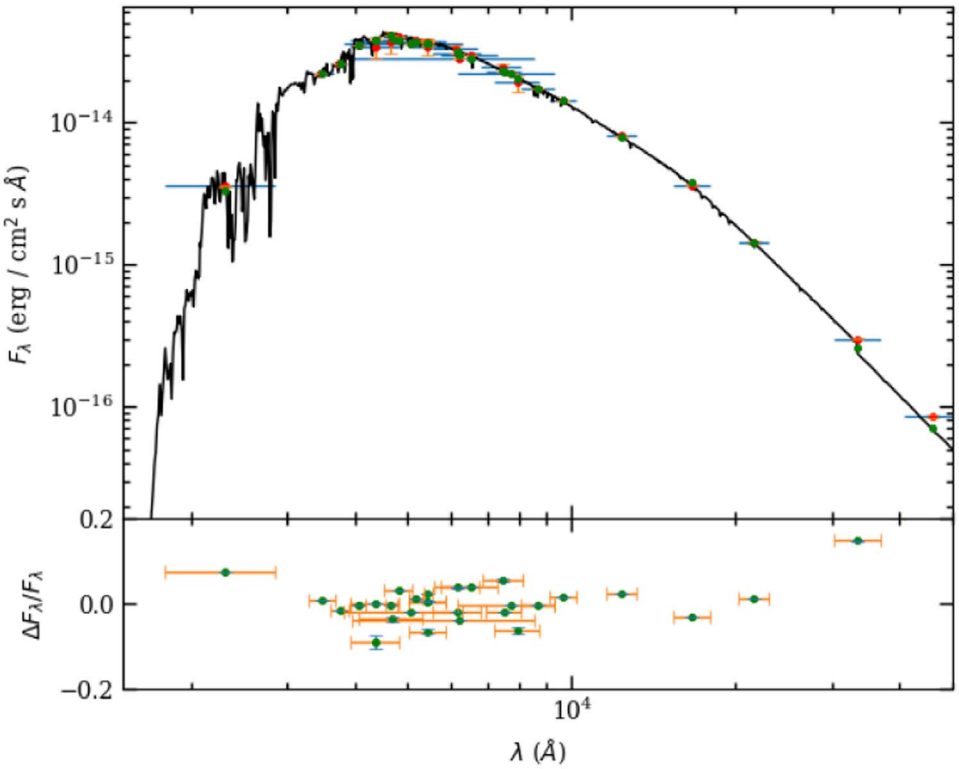

Figure 7. Top: SED for PLA 255, the proxy for DS And B (red points) and a fitted ATLAS9 model for $T_{\rm eff} = 6290$ K (solid line, and green points for integrations over filter response curves). Horizontal error bars represent the effective width of the filter. Bottom: fractional difference between the stellar fluxes and the best-fit fluxes for the ATLAS9 (green) model.

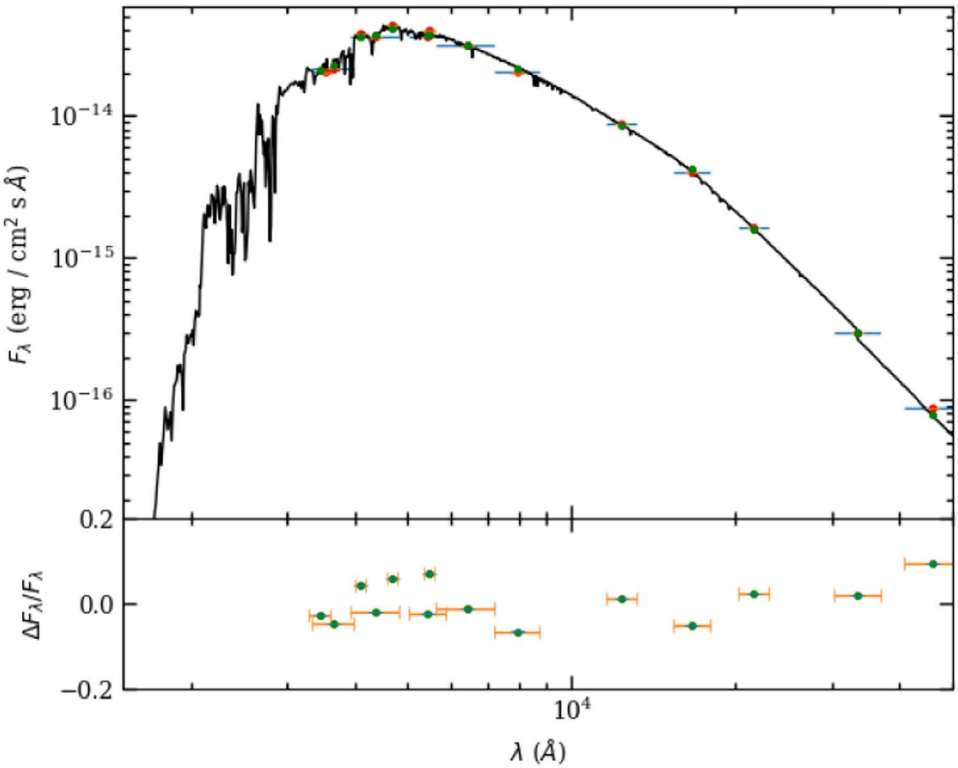

Figure 8. Top: SED for DS And B (red points) and a fitted ATLAS9 model for $T_{\rm eff} = 6100$ K (solid line, and green points for integrations over filter response curves). Horizontal error bars represent the effective width of the filter. Bottom: fractional difference between the stellar fluxes and the best-fit fluxes for the ATLAS9 (green) model.

contamination, although this did not appear to affect the measurement of the binary star velocities.

We also reanalyzed 15 observations of DS And taken using the Fiber-fed Echelle Spectrograph (FIES; Telting et al. 2014) on the 2.56 m Nordic Optical Telescope (NOT) in 2007 August, and 2008 July–November. These spectra were taken by Th. Mellergaard Amby, S. Frandsen, or NOT support staff. Exposures were 1200 s (with one exception of 1800 s) taken using the medium resolution fiber setup. The spectra were processed using the standard reduction pipeline FIEStool.[11]

For the HRS spectra, we conducted a spectral disentangling (González & Levato 2006) to iteratively determine separated averaged spectra for the two stars in the binary and their radial velocities at each epoch. Figure 9 shows the combined broadening function for one spectrum. Radial velocities were derived from fits of rotational broadening profiles to the broadening functions (Rucinski 1992) derived from companion-subtracted spectra. Synthetic spectral templates from Coelho et al. (2005) with temperatures of 6750 and 6000 K were used for the primary and secondary star, respectively. We derived our final radial velocities from a disentangling involving the entire spectral range between 4825 and 5760 Å. In order to get an empirical estimate of the velocity uncertainties, we disentangled on three sections of the spectrum of roughly 300 Å and computed the error in the mean.

FIES spectra cover wavelengths between 3700 and 7300 Å in 78 spectral orders, but the bluest and reddest orders were removed (due to low signal-to-noise ratio and large sky contamination, respectively). We attempted to find a middle ground between having multiple measurements of the velocity from each spectrum (for the purpose of understanding velocity uncertainties from the measurement scatter) and signal in the broadening functions (from using larger wavelength ranges to reduce noise). We settled on six sections of approximately 300 Å each (4060–4330, 4329–4630, 4611–4952, 4950–5270, 5251–5523, and 5506–5860 Å), generally including one strong line. Although these ranges overlap somewhat, in all cases the sections were extracted from separate orders of the spectrum. Orders were continuum normalized separately before being merged together using the IRAF task scombine. We fit rotational broadening profiles for both stars using a modified version of the Python code BF-rvplotter.[12] With two exceptions the broadening functions for the two stars were separately resolved. One spectrum was removed from consideration because the binary was in eclipse at the time of observation, and reliable broadening function fits could not be obtained as a result. In a second case, the broadening function of the secondary star strongly overlapped that of the primary, and only the primary could be reliably measured.

After comparison with the radial-velocity measurements from HET HRS, we found noticeable differences in the velocity curves. We re-examined the FIES spectra and found that strong terrestrial lines (the [O I] emission line at 557.33 nm, and the O_2 absorption band at 627.6 nm) showed an offset from their expected values. We therefore cross-correlated these orders against a spectrum from 2007 to derive a correction for the velocities. The corrections ranged between −2.3 and −7.8 km s^{-1} for six spectra. With one exception, these spectra were taken between phases of 0.1 and 0.4. Because the FIES velocities from Amby Ottosen (2011)

[11] http://www.not.iac.es/instruments/fies/fiestool/FIEStool.html

[12] https://github.com/mrawls/BF-rvplotter

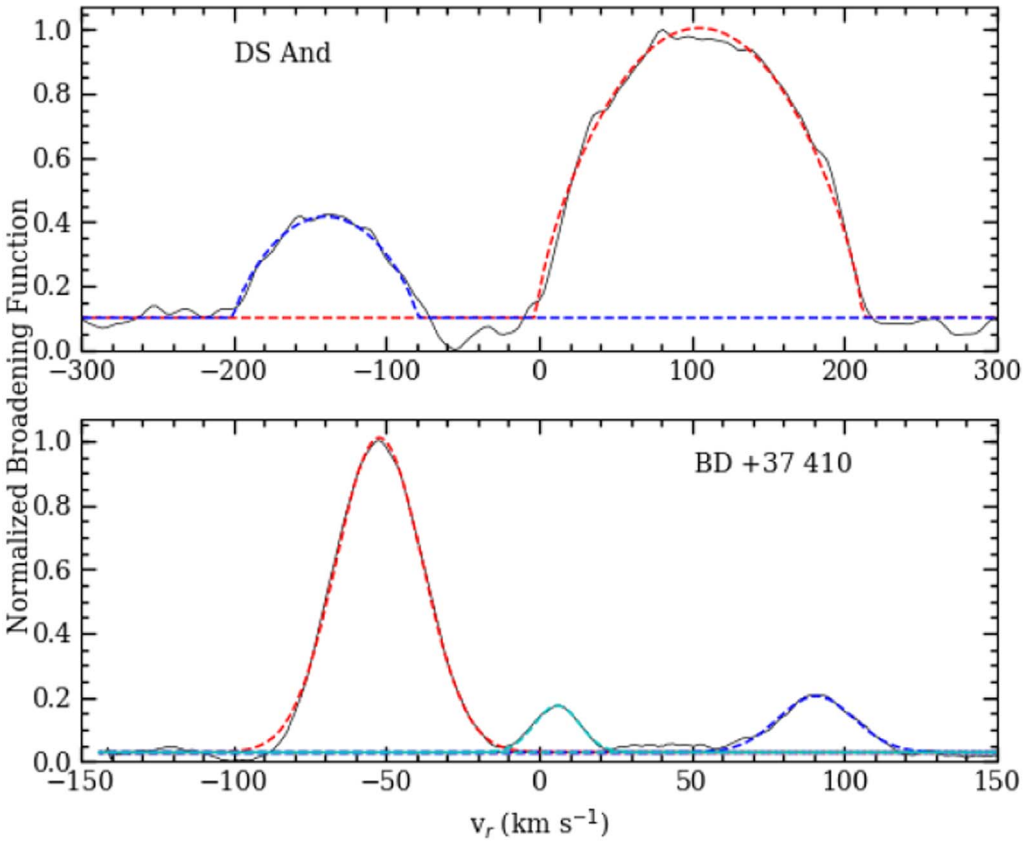

Figure 9. Example broadening functions for the binaries. Primary star fits are in red, secondary star fits in blue, and tertiary star fits in cyan. Top panel: DS And broadening function from an HET HRS spectrum for HJD 2,455,811.801, with fits of rotational broadening functions with $v_{\rm rot}\sin i$ = 106.6, 59.7 km s^{-1}. Bottom panel: BD +37 410 broadening function from a WIYN Hydra spectrum for HJD 2,452,140.878, with Gaussian fits with σ = 14.1, 12.4, and 7.3 km s^{-1}.

constituted a third of the measurements used by Milone et al. (2019) in their analysis, we believe this resulted in a significant systematic error in their mass determinations. The complete set of radial velocities is given in Table 9.

The rotational broadening was determined for each star from the broadening function fits, and we found these to be 105 ± 0.7 and 58.3 ± 0.8 km s^{-1}, respectively for the primary and secondary stars. The quoted uncertainties are errors in the mean of the rotational broadenings measured from each spectrum. For comparison, Milone et al. (2019) found 106 ± 3 and 62 ± 2 km s^{-1} for the two stars from the FIES spectra. As Milone et al. (2019) also found, these values are approximately consistent with synchronous rotation for the binary. This is 27% of breakup speed for the primary, and 13% for the secondary.

As shown in Figure 10, the rotational velocities put these stars as comfortably rotating faster than other single stars at the same brightness level in the cluster (Mermilliod et al. 2009), even accounting for inclination effects. The stars of DS And are at magnitude levels where the cluster main-sequence stars have separate maximums in lithium abundance (Boesgaard et al. 2022). Determination of Li abundances for the DS And stars are complicated by the rotational velocities, but the primary star at least appears to have had some Li depletion. The average spectrum of DS And A derived from a disentangling of the NOT FIES spectra is shown in Figure 11. Fe, Ca, and Si lines are seen, but Li absorption is not obvious. This depletion is probably a sign of rotationally driven mixing in the star, but further analysis is beyond the scope of the paper.

3.3.2. BD +37 410

For BD +37 410, our primary source for velocity measurements was previously unpublished spectra taken with Hydra multifiber echelle spectrograph on the 3.5 m WIYN telescope at Kitt Peak National Observatory between 2001 August 18 and 2009 September 30. The spectra covered 4990–5250 Å near the Mg I b triplet. Typically, 8–10 exposures of around 1800 s were taken each night of observations, and had high signal-to-noise ratios. After some experimentation, we settled on the 4990–5177 Å range for our analysis as this appeared to provide the best signal on the fainter secondary star. We computed broadening functions from each spectrum using a synthetic template with $T_{\rm eff} = 6500$ K and $\log g = 4.0$ from Coelho et al. (2005), and fitted components with Gaussians. An example broadening function and fit is shown in Figure 9.

We were able to clearly detect the secondary star in all spectra with sufficient velocity separation, but in addition we found a third component with a radial velocity of 5–7 km s^{-1}, near the cluster mean and the binary systemic velocity γ. There are no other known sources likely to be contaminating the fiber aperture, so it is likely that the third object is associated with the binary, especially considering the large extent of the cluster on the sky. We can get a rough idea of the luminosity ratios for the stars from measurements of the broadening function areas if the temperatures of the components are similar. We find averages $A_2/A_1 = 0.148 \pm 0.003$ and $A_3/A_1 = 0.088 \pm 0.002$ (error in the mean) from 44 observations. This implies that the secondary star contributes approximately 12% of the system light in the optical, and the tertiary star contributes approximately

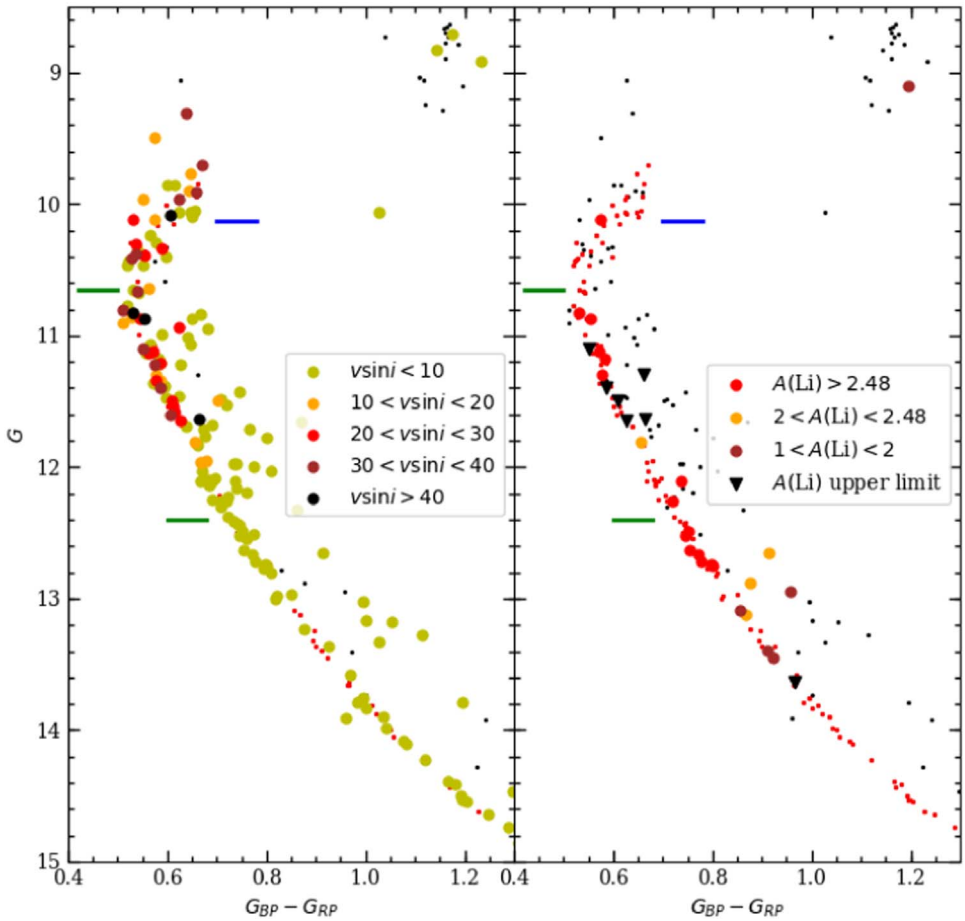

Figure 10. Gaia CMDs with (left panel) rotational velocity and (right panel) Li abundance information. Gaia-selected likely binary members are shown with small black points, and photometrically selected single-star members in red. Approximate G magnitudes of the DS And components are shown with green lines, and BD +37 410 is shown with a blue line.

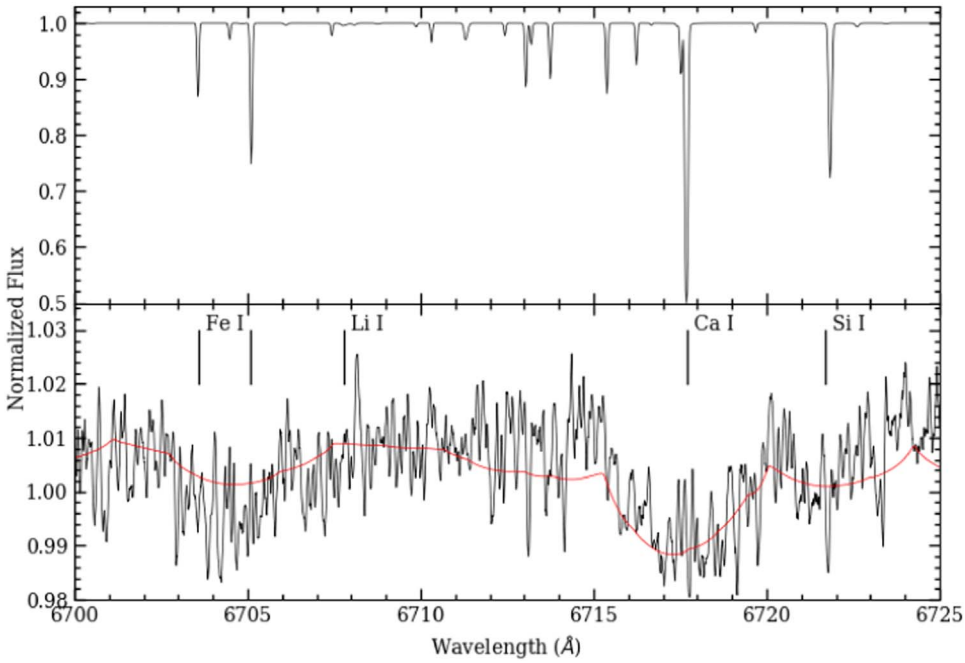

Figure 11. Top panel: synthetic spectrum for $T_{\rm eff} = 6750$ K from Coelho et al. (2005). Bottom panel: disentangled average spectrum of DS And A from NOT FIES observations in the region of the 6707.8 Å Li I line, with other strong lines identified. The rotationally broadened synthetic spectrum (using $v_{\rm rot} \sin i = 105$ km s^{-1}) is shown in red for comparison.

7%. We will use this information to understand the eclipse depth in the analysis below, but it allows us to also identify a single cluster member star (PLA 641) as a rough proxy for the primary star based on its brightness relative to the binary.

We also made use of literature radial-velocity measurements for the system. Pribulla et al. (2010) recorded 18 spectra with CfA Digital Speedometers (Latham 1992), reanalyzed using two-dimensional cross correlation via TODCOR (Zucker & Mazeh 1994). Mermilliod et al. (2009) recorded 32 spectra with the photoelectric scanner CORAVEL (Baranne et al. 1979; Mayor 1985) on the Swiss 1 m telescope at Observatoire de Haute-Provence. Two additional measurements of the primary star were pulled from Pribulla et al. (2009), who observed the system with the slit spectrograph at the 1.88 m telescope of the David Dunlop Observatory. The radial velocity was measured from broadening functions derived from a comparison with an observed sharp-line spectral template. Finally, three velocity measurements were available from the LAMOST Data Release 4 (Tian et al. 2020). Two of the measurements with radial velocities near zero were clearly discrepant with the radial-velocity curve and were discarded. None of these velocity data sets have previously been analyzed together. The radial velocities that were used in modeling are given in Table 9. We note that Mermilliod et al. measured the rotational speed of the primary star as $v_{\rm rot} \sin i = 19.1 \pm 1.6$ km s^{-1}, in line with other upper main-sequence stars.

4. Analysis

4.1. Cluster Membership

Milone et al. (2019) discussed the membership of DS And and came to the conclusion that the system is a likely member based on sky location, CMD locations of the component stars, distance, extinction and metallicity, radial velocity, and proper motion. Here, we update a few pieces of information related to membership.

We find that the systemic radial velocity γ of DS And from both spectroscopic data sets are fully consistent with recent mean cluster velocity measurements. Pilachowski et al. (1988) found a mean velocity of 4.9 ± 0.7 km s^{-1} from six stars. Daniel et al. (1994) found a mean of 5.5 ± 0.6 km s^{-1} from a larger sample of 33 stars. Mermilliod et al. (1998) found a mean of 4.68 ± 0.11 km s^{-1} from 15 cluster giants. Milone et al. (2019) found a larger systemic velocity for DS And ($8.13 \pm 0.02 \pm 0.50$ km s^{-1}) from velocities derived from the FIES spectra, and this was consistent with older measurements of the cluster velocity (Rebeirot 1970; Friel et al. 1989). As we pointed out earlier, however, several of these measurements were affected by zero-point errors, and our newer determination of γ is much more consistent with the cluster mean.

In proper motions, Agüeros et al. (2018) determined a membership probability of 99.8% by modeling field and cluster stars from ground-based measurements. Cantat-Gaudin et al. (2018) determined DS And to be a 100% member from Gaia Data Release 2 measurements of the clustering of proper-motion and parallax values.

For BD +37 410, ground-based membership surveys (Francic 1989; Platais 1991; Daniel et al. 1994) have identified the star as a clear cluster member. With the availability of Gaia data, the membership is a little more ambiguous. While Agüeros et al. (2018) identified the star as a cluster member, Cantat-Gaudin et al. (2018) did not, most likely due to a proper motion in the R.A. direction ($\mu_{\alpha^*} = 10.99 \pm 0.12$ mas yr^{-1}) that is slightly larger than for most members (the cluster average is $\mu_{\alpha^*} = 9.8$ mas yr^{-1}; Gaia Collaboration et al. 2018). Bhattacharya et al. (2021) also did not identify the star as a possible member in their survey for stars in tidal tails, but the binary was outside of their search range in μ_{α^*}. Boffin et al. (2022) identified the binary as a member in their wider search for tidal features of the cluster. BD +37 410 is only 0°.22 from the cluster center on the sky, and deviations from cluster means in other quantities are small: the parallax (2.28 ± 0.12 mas for the binary, versus 2.23 mas for the cluster), proper motion in the decl. direction (-12.17 ± 0.11 mas yr^{-1}, versus -11.76 mas yr^{-1}), and radial velocity (4–6 km s^{-1} from our analysis, versus similar values for the cluster from the studies listed above). In addition, the binary's photometry puts it solidly among other cluster members at the bright end of the main sequence. As a result, we believe the evidence points clearly toward membership.

4.2. Binary Star Modeling

4.2.1. DS And

We used the Eclipsing Light Curve code (ELC; Orosz & Hauschildt 2000) to simultaneously model the radial velocities and multiband photometry for DS And. We used a differential evolution Markov Chain optimizer (Ter Braak 2006) for seeking the overall best-fit model and exploring parameter space around that model to generate a posterior probability sampling. For the purposes of gauging some of the possible systematic errors, we conducted runs with different modeling runs approaches.

As a first model, we fitted the radial-velocity data alone. Two of the parameters were the orbital period P and a reference time of primary eclipse t_c. Four additional parameters mostly characterize the velocity variation: the velocity semiamplitude of the primary star K_1, mass ratio $q = M_2/M_1 = K_1/K_2$, and systematic radial velocities[13] γ_1 and γ_2. We have also allowed for a difference in zero-point between the velocities from FIES and HRS spectra. Previous examination of the times of secondary minimum has not revealed evidence of nonzero eccentricity (Schiller & Milone 1988). Because the binary has such a small orbital separation, tidal effects are assumed to maintain the system at zero eccentricity.

The subsequent model runs also utilized light-curve data. These improve the precision of measurements of period P and reference time t_c, but require additional fitting parameters. Because the stars orbit closely enough for tidal distortion of their surfaces, we used Roche-lobe filling factors f_1 and f_2 in modeling the stellar sizes and out-of-eclipse light variations. The orbital inclination i and temperature ratio T_2/T_1 are primarily determined by eclipse data. The primary star temperature T_1 was included as a fitting parameter as well, but is only weakly constrained by the light curves, and we consider the primary constraints on it to come from the SED fitting described earlier in Section 3.2.1.

We included a parameter to account for potential contamination of the TESS light curve by nearby stars. We find that this parameter is not constrained in the models, but we allow it to vary in a range 0.05 ± 0.05 to account for this uncertainty in the fitting. For perspective, the TESS Input Catalog (v. 8.2; Stassun et al. 2019) gives a contamination fraction of 0.0012

[13] We allow for the possibility of differences for the two stars that could result from differences in convective blueshifts or gravitational redshifts.

Table 5
Best-fit Model Parameters for DS And

Parameter	This Paper					M19
	RVs and LCs				RVs Only	
	LDC	albedo	ATM	albedo		
Constraints:						
T_1 (K)	7070 ± 150					
T_2 (K)	6100					
γ (km s^{-1})						$8.13 \pm 0.02 \pm 0.50$
$\gamma_{1,\mathrm{NOT}}$	4.63 ± 0.03	4.58 ± 0.03	4.54 ± 0.03	4.59 ± 0.03	5.25 ± 0.33	
$\gamma_{1,\mathrm{HET}}$	5.14 ± 0.12	5.32 ± 0.12	5.44 ± 0.12	5.29 ± 0.12	5.32 ± 0.13	
$\gamma_{2,\mathrm{NOT}}$	5.35 ± 0.10	5.22 ± 0.10	5.08 ± 0.10	5.21 ± 0.10	4.88 ± 0.30	
$\gamma_{2,\mathrm{HET}}$	3.77 ± 0.28	4.18 ± 0.28	4.59 ± 0.28	4.15 ± 0.28	3.52 ± 0.26	
P (days)	1.01051956	1.01051955	1.01051956	1.01051955	1.0105217	1.010518870
σ_P (days)	2.0×10^{-8}	2.0×10^{-8}	2.0×10^{-8}	2.0×10^{-8}	1.4×10^{-6}	2.5×10^{-8}, 1.20×10^{-7}
t_c−2,400,000	55,486.7694	55,486.76941	55,486.76941	55,486.76942	55,486.7676	36,142.40281
σ_{t_c}	0.00004	0.00005	0.00004	0.00004	0.0006	0.00027, 0.00114
$q = M_2/M_1$	0.705 ± 0.003	0.700 ± 0.003	0.699 ± 0.003	0.695 ± 0.003	0.707 ± 0.003	0.657 ± 0.001
K_1 (km s^{-1})	124.28 ± 0.31	123.86 ± 0.32	123.98 ± 0.32	123.47 ± 0.32	124.17 ± 0.30	119.75 ± 0.98
K_2 (km s^{-1})	182.00 ± 0.52				175.58 ± 0.59	176.36 ± 0.77
i (°)	$85.49^{+0.07}_{-0.11}$	$85.99^{+0.12}_{-0.16}$	$85.51^{+0.26}_{-0.09}$	$86.18^{+0.08}_{-0.14}$		$89.35 \pm 0.19 \pm 0.45$
f_1	0.7425 ± 0.0009	0.7335 ± 0.0015	0.7417 ± 0.0011	0.7329 ± 0.0014		
f_2	0.4389 ± 0.0010	0.4395 ± 0.0009	0.4350 ± 0.0012	0.4355 ± 0.0008		
T_1 (K)	6900 ± 10	6771 ± 10	6855 ± 16	6770 ± 7		
T_2/T_1	0.8822 ± 0.0006	0.8881 ± 0.0009	0.8819 ± 0.0005	0.8869 ± 0.0008		
contam (TESS)	0.05 ± 0.05					
a_1		0.20 ± 0.06		0.22 ± 0.06		
a_2		$0.05^{+0.04}_{-0.03}$		0.13 ± 0.04		
$M_1/M_\odot$	1.682 ± 0.013	1.688 ± 0.013	1.695 ± 0.013	1.702 ± 0.013		$1.655 \pm 0.003 \pm 0.030$
$M_2/M_\odot$	1.186 ± 0.008	1.181 ± 0.008	1.187 ± 0.007	1.183 ± 0.007		$1.087 \pm 0.005 \pm 0.040$
$R_1/R_\odot$	2.188 ± 0.006	2.175 ± 0.006	2.196 ± 0.006	2.181 ± 0.006		$2.086 \pm 0.003 \pm 0.013$
$R_2/R_\odot$	1.205 ± 0.004	1.205 ± 0.004	1.195 ± 0.004	1.195 ± 0.003		$1.255 \pm 0.005 \pm 0.012$
log g_1 (cgs)	3.984 ± 0.0013	3.990 ± 0.0015	3.985 ± 0.0013	3.992 ± 0.0016		
log g_2 (cgs)	4.351 ± 0.0018	4.349 ± 0.0018	4.358 ± 0.0023	4.357 ± 0.0017		
$L_1/L_\odot$	9.80 ± 0.08	9.02 ± 0.08	9.60 ± 0.11	9.05 ± 0.06		$9.58 \pm 0.12 \pm 0.20$
$L_2/L_\odot$	1.80 ± 0.014	1.72 ± 0.013	1.72 ± 0.019	1.68 ± 0.012		$1.77 \pm 0.03 \pm 0.06$

Note. "LDC": limb-darkening coefficient fitting. "ATM": atmospheric model fitting. "albedo": fitting for reflection albedo coefficients for the two stars. See Section 4.2.1 for parameter definitions.

for DS And. We note that our models of the TESS light curves account for the long integration time in the full-frame images by integrating the computed light curves in each observed exposure window.

In two runs (labeled "albedo" in Table 5), we experimented with fitting bolometric albedo coefficients a_1 and a_2 related to the reflection effect. The coefficient is expected to be 1 for stars with a radiative envelope and 0.5 for stars with a convective envelope. The secondary star in DS And probably has a thin surface convection zone that we thought might affect the strength of the reflection effect. In fact, our fits point toward low values for the coefficients of both stars. The allowance for the lower coefficients seems to have the largest effect on the radius of the primary star, reducing it by about 0.6%.

In two of our runs (with and without albedo coefficient fitting), we allowed limited fitting for limb-darkening coefficients (labeled "LDC" in Table 5). In these runs, we fit for two quadratic limb-darkening law coefficients for each star in each filter band. We used coefficients in the form recommended by Kipping (2013) to produce a well-defined area of parameter space that has physically realistic values where each model star is forced to darken toward its limb with a concave-down darkening curve. If we allow the limb-darkening coefficients to fully float within the physically realistic region, however, the limb-darkening coefficients take on values that are more appropriate for stars with temperatures outside the range from our SED constraints, according to theoretical models. As a result, we decided to constrain the coefficients to small ranges near the expected values from Claret et al. (2013) and Claret (2018) based on the stellar temperatures inferred from SEDs.

Finally, we conducted runs where limb-darkening coefficient fitting was replaced with angular-dependent intensity profiles derived from model atmospheres for the appropriate T_{eff} and $\log g$ (labeled "ATM" in Table 5). While this utilizes information from detailed atmospheres, there still remains the possibility of systematic errors in those calculations.

The quality of the fitting is quantified by an overall χ^2 derived from comparing the radial-velocity and light-curve data to the models, as well as from how well an a priori constraint on the primary star temperature (from SED fitting of single stars at the cluster turnoff) was matched. To try to ensure that different data sets were given appropriate weights in the models, we empirically scaled uncertainties on different data sets to produce a reduced χ^2 of 1 relative to a best-fit model

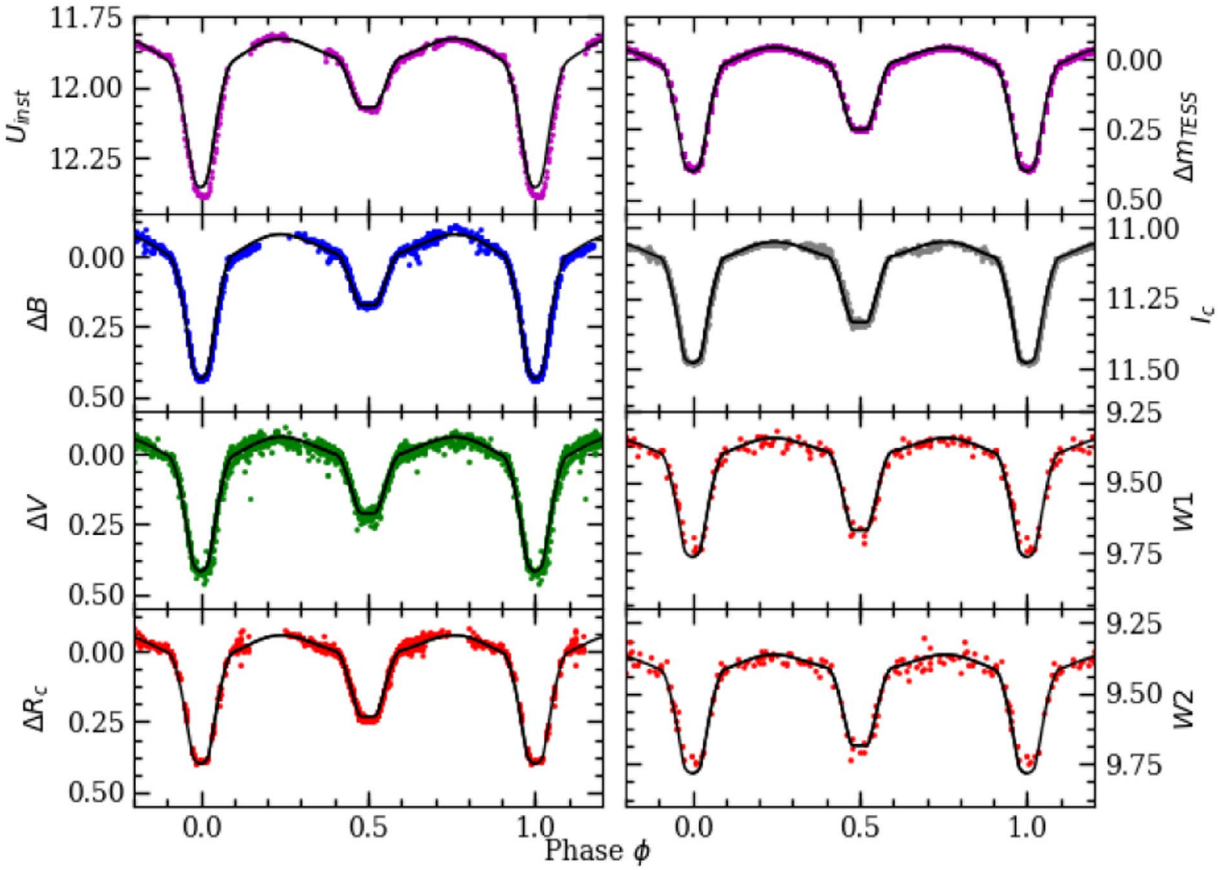

Figure 12. Phased photometry for DS And compared with the best-fit binary models. B, V, R_C, and TESS light curves are zero-pointed to the magnitude at eclipse ingress/egress phases. W1 and W2 photometry is in calibrated magnitudes. The U curve is in instrumental magnitudes.

when the particular data set was fit on its own. For spectroscopic velocity measurements, this meant scaling subsets of the data differently according to the source spectrograph and the star (primary and secondary).

Approximate 1σ parameter uncertainties were derived from the parts of the posterior distributions containing 68.2% of the remaining models from the Markov chains. Gaussians were good approximations to the posterior distributions for all parameters except limb-darkening coefficients and the inclination (which showed a small bimodality). The results of the parameter fits are provided in Table 5.

A comparison of the light curves with the best-fit model are shown in Figure 12, and a comparison of the radial-velocity measurements with models are shown in Figure 13. The fitting runs we present used photometry in eight filter bands: $UBVR_CI_C$, TESS, and WISE W1 and W2 (Chen et al. 2018). The fits were generally very good with the exception of the primary eclipse depth for the bands at the extremes of the wavelength range (U and W2).

The systematic differences for the fitted masses and radii from run to run generally exceed the statistical uncertainties, so that we consider both when assessing uncertainty. For the comparison, we use the mean of masses and radii from the four radial-velocity and light-curve fitting runs: $M_1/M_\odot = 1.692 \pm 0.004 \pm 0.010$, $R_1/R_\odot = 2.185 \pm 0.004 \pm 0.008$, $M_2/M_\odot = 1.184 \pm 0.001 \pm 0.003$, and $R_2/R_\odot = 1.200 \pm 0.003 \pm 0.005$. In these values, the uncertainties are statistical and systematic (indicated by run-to-run deviations), respectively.

4.2.2. BD +37 410

Modeling of this binary system utilized the same ELC program, but the fitted parameters differed because of the configuration of the system. The stars were assumed to be spheres, in contrast to DS And. We fitted the radial-velocity data sets and TESS light curve simultaneously with twelve parameters: orbital period P, reference time of periastron t_0, velocity semiamplitude of the primary star K_1, mass ratio $q = M_2/M_1 = K_1/K_2$, eccentricity e, argument of periastron ω, inclination i, the sum of the radii $(R_1 + R_2)/R_\odot$, the radius ratio R_1/R_2, the surface area ratio of the primary relative to the tertiary, and two quadratic limb-darkening parameters for the eclipsed secondary star. The last three parameters relate to the modeling of the eclipse light curve but are poorly constrained by the data. We allow some variation around our best-estimated values in order to allow those uncertainties to propagate into the uncertainties for other parameters. We also fitted for systematic radial velocities γ for each star in each data set to allow for instrumental zero-point differences and astrophysical effects (such as differences in convective blueshifts or gravitational redshifts between the stars).

We allowed for a small amount (1.52%) of light contamination of the TESS aperture due to a few faint nearby stars. The value was taken from the TESS Input Catalog (Stassun et al. 2018, v. 8.2) and makes use of data from Gaia DR2. As was the case with DS And, this parameter is not constrained in the models, but we allow it to vary in a range 0.015 ± 0.005 to account for this uncertainty in the fitting. The contamination

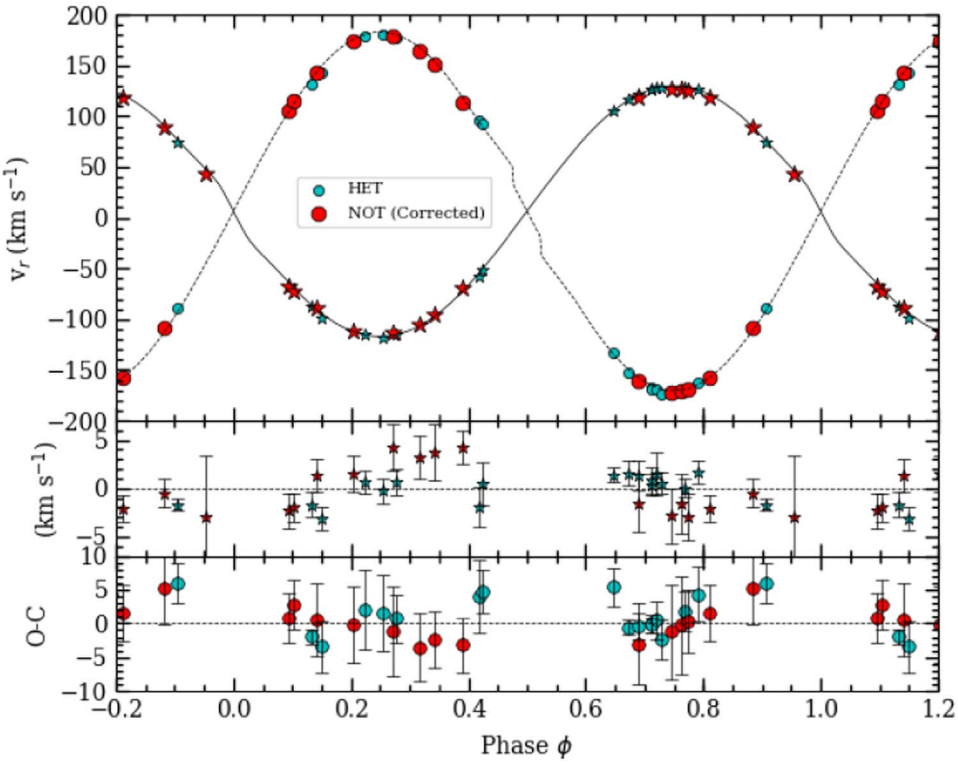

Figure 13. Top panel: radial velocities of the stars of DS And, phased to the orbital period, along with best-fit models. Bottom panels: $(O - C)$ residuals for the radial velocities.

has a minimal effect on the fitted parameters, however. The "third light" contribution of the tertiary star seen in spectra is a more substantial effect.

The SED temperature measurement from the binary's combined light gives a lower limit to the temperature of the primary star ($T_1 > 6480$ K). We further estimated the CMD positions of the three stars assuming that they were all single-star cluster members with brightnesses consistent with our broadening function estimates from Section 3.3. Using SED fits to stars at those levels, we find $T_1 = 6620$ K, $T_2 = 6330$ K, and $T_3 = 6200$ K.[14] These temperatures guided our selection of the ranges the limb-darkening coefficients were allowed to vary in, and the relative sizes of the primary and tertiary stars.

As a final note, we see evidence that primary star radial velocities near aphelion ($0.45 < \phi < 0.60$) showed systematic deviations of up to 5 km s^{-1} away from the best-fit model toward the tertiary star velocity, and in some cases, also the secondary star velocity. This seemed to be clear evidence that the primary star's velocity measurements were biased when the secondary star's lines were not separately resolved. As a result, we left these measurements out of the final fitting because they had a demonstrable effect on the star masses.

The results of the fitting are shown in Table 6, and model comparisons are shown in Figures 14 and 15. Although the system only has one partial eclipse per orbit, the inclination is well constrained. In a crude sense, the inclination is restricted to a range of values in which the eclipse occurs and is not total. Practically though, the eclipse reaches a depth that is close to what it would be for a total eclipse (approximately 12%), so the light curve constrains the inclination to a much smaller range.

4.3. Comparisons with Models

4.3.1. Luminosity and Temperature

The calibrated photometry for DS And, along with measurements of the depth of the total secondary eclipse, allowed us to identify the contributions of both stars to the flux in many wave bands in Section 3.2.1. In turn, this allowed us to fit the SED and derive the effective temperatures and bolometric fluxes, as well as luminosities in combination with the cluster distance. For BD +37 410, the primary star is the dominant contributor to the binary's light, making it easier to assess its characteristics directly from the SED.

Figure 16 shows a comparison of the components of these binaries with isochrones in the mass–luminosity plane. With respect to BD +37 410 A, most models are ruled out because the model star leaves the turnoff and moves onto the subgiant branch before it reaches the observed luminosity, in disagreement with the observations. This is a symptom of error in the convective core overshooting parameters, and will be discussed in the next subsection.

A striking aspect of this plot with regard to DS And is that the luminosity of the primary star is substantially lower than the models for any reasonable age at the measured mass.[15] Even though DS And A appears to be at the turnoff for NGC 752, the star's mass–luminosity combination is systematically off from the locus for turnoff stars predicted by different isochrone sets.

[14] The template temperature used for the secondary star by Pribulla et al. (2010), 6750 K, is unlikely to be correct. If the secondary star were that hot, it would likely require that the primary star reside off the cluster main sequence in order to match the observed photometry of the binary star. Their temperature for the primary star (6500 K) is, however, close to our determination.

[15] The measurements of Milone et al. (2019) put the primary closer to the isochrones (due to a lower mass and higher luminosity), but it is still significantly subluminous compared to the models.

Table 6
Best-fit Model Parameters for BD +37 410

Parameter	This Paper	P10
Constraints:		
T_1 (K)	6620	6500
T_2 (K)	6330	6750
T_3 (K)	5950	
contam. (TESS)	0.015 ± 0.005	
$\gamma_{1,\mathrm{COR}}$	5.96 ± 0.04	
$\gamma_{1,\mathrm{CfA}}$	4.75 ± 0.05	4.70 ± 0.33
$\gamma_{1,\mathrm{WIYN}}$	6.03 ± 0.03	
$\gamma_{2,\mathrm{COR}}$	$3.83^{+0.09}_{-0.05}$	
$\gamma_{2,\mathrm{CfA}}$	$5.96^{+0.07}_{-0.08}$	
$\gamma_{2,\mathrm{WIYN}}$	5.35 ± 0.07	
P (days)	15.534837	15.53446
σ_P (days)	$^{+0.000007}_{-0.000006}$	0.00092
t_P–2,400,000	45,680.165	48,491.979
σ_{t_P}	$^{+0.007}_{-0.008}$	0.037
q	0.684 ± 0.002	0.689 ± 0.020
K_1 (km s^{-1})	56.99 ± 0.08	57.03 ± 0.54
K_2 (km s^{-1})	83.3 ± 0.22	82.8 ± 1.5
e	$0.5142^{+0.0006}_{-0.0012}$	0.5156 ± 0.0054
ω (°)	259.9 ± 0.2	260.6 ± 1.3
i (°)	$81.7^{+0.07}_{-0.06}$	76–83
$M_1/M_\odot \sin^3 i$	1.664 ± 0.010	1.638 ± 0.076
$M_2/M_\odot \sin^3 i$	1.139 ± 0.005	1.129 ± 0.037
$M_1/M_\odot$	1.717 ± 0.011	
$M_2/M_\odot$	1.175 ± 0.005	
$(R_1 + R_2)/R_\odot$	4.085 ± 0.017	
R_1/R_2	$2.44^{+0.16}_{-0.11}$	
$R_1/R_\odot$	2.899 ± 0.013	
$R_2/R_\odot$	1.186 ± 0.005	
log g_1 (cgs)	3.748 ± 0.004	
log g_2 (cgs)	4.360 ± 0.003	

Model comparisons also indicate that DS And A is systematically cooler than the model predictions for a turnoff star of its mass, regardless of the isochrones used. The amount of core overshooting has very little effect on these conclusions. Overshooting shifts turnoff masses and temperatures in such a way as to leave the relation the same, with only a change in the corresponding age for a given turnoff mass. The resolution of the luminosity disagreement must be elsewhere.

The temperature discrepancy could be solved and the luminosity discrepancy could be alleviated (but not fixed) if the bulk metallicity of the cluster stars were higher, as shown in Figure 17. As yet, there is no evidence that diffusion is affecting NGC 752 stars in such a way as to make their surface metal abundances appear lower than the bulk metallicity—main-sequence and red giant stars appear to have the same abundances (Lum & Boesgaard 2019). But a higher solar metal abundance $Z_\odot$ could produce a similar result without substantially affecting the radius comparisons in the previous section. As we will see below, a higher metal content for cluster stars throws models out of agreement with the observed main sequence. We are left with the impression that DS And A's luminosity is systematically different than reasonable model predictions.

This result rests in part on the fact that we can constrain the age and/or evolutionary state of the star as well as its metallicity because the binary is a member of the NGC 752 cluster. We can further test the luminosity of the primary star by comparing with other well-studied eclipsing binary stars of similar mass (see Table 7 and Figure 18), although these generally do not have supporting information that is as complete.

As shown in the mass–luminosity comparison in Figure 18, DS And A falls among stars of similar mass, but has a luminosity much smaller than predicted for a presumed cluster age of around 1.5 Gyr. An HR diagram (Figure 19) emphasizes the unusual combination of characteristics for DS And A though—while the other stars in Table 7 fall near an evolution track for DS And A's mass, DS And A itself is significantly redder and/or less luminous. The stars that are likely to be most evolved (based on a larger radius and lower temperature, such as EI Cep B; Torres et al. 2000) have higher luminosities. The coolest of the stars in Table 7 (IO Aqr B) stands out, however. This star is in a relatively short-period orbit and is the largest of the stars in the table. Graczyk et al. (2015) were able to model both stars in the binary with an isochrone of the same age, but only if they used an extremely supersolar metallicity [M/H] = +0.3 without spectroscopic evidence to justify this. This is potentially a symptom that the stars are less luminous than standard evolution models predict (and that the metallicity must be increased to compensate). If true, it may be another indication that stars in close binaries can have lower-than-expected luminosities and effective temperatures, due in some way to their tidal interactions.

4.3.2. Mass and Radius

High-precision measurements of mass and radius from evolved stars in detached eclipsing binaries are capable of constraining age in a way that is independent of distance and reddening. The cases of the two binaries here are somewhat complicated, however. For DS And, there are questions about how strongly the stellar characteristics have been influenced by star–star interactions, whether through the tidal interactions or through an unusual past history. For BD +37 410, the lack of a secondary eclipse means that the individual stellar radii are somewhat poorly measured, although the sum of the radii is constrained. In both cases it is helpful to have radius comparisons.

Photometric radii can be derived from SED fits for bolometric flux and effective temperature, along with precise distances from Gaia. Calculations for our sample of single-star candidates are shown in Figure 20. If we estimate the radius of the secondary star in BD +37 410 from stars at the appropriate brightness level, we have $R_2 = 1.14 R_\odot$, which implies $R_1 = 2.92 R_\odot$ when we subtract from the radius sum from the binary fitting. These values are consistent with the results from binary fitting in Table 6.

Even with the uncertainties, BD +37 410 A is reliably seen to be a great deal larger than the primary star of DS And, and, importantly, it has reached its present size while still on the main sequence. BD +37 410 A sits among a large number of other stars in CMDs such as in Figure 10, clearly showing that its evolutionary timescale is still slow and nuclear—the cluster itself does not have any subgiants that are likely to be single stars because the evolution is too rapid there. While all reasonably isochrone models will have a star with the mass of BD +37 410 reach a radius of $2.9 R_\odot$ at some point, the encoded physics in the isochrones determines whether it happens as a late main-sequence star or as a rapidly evolving

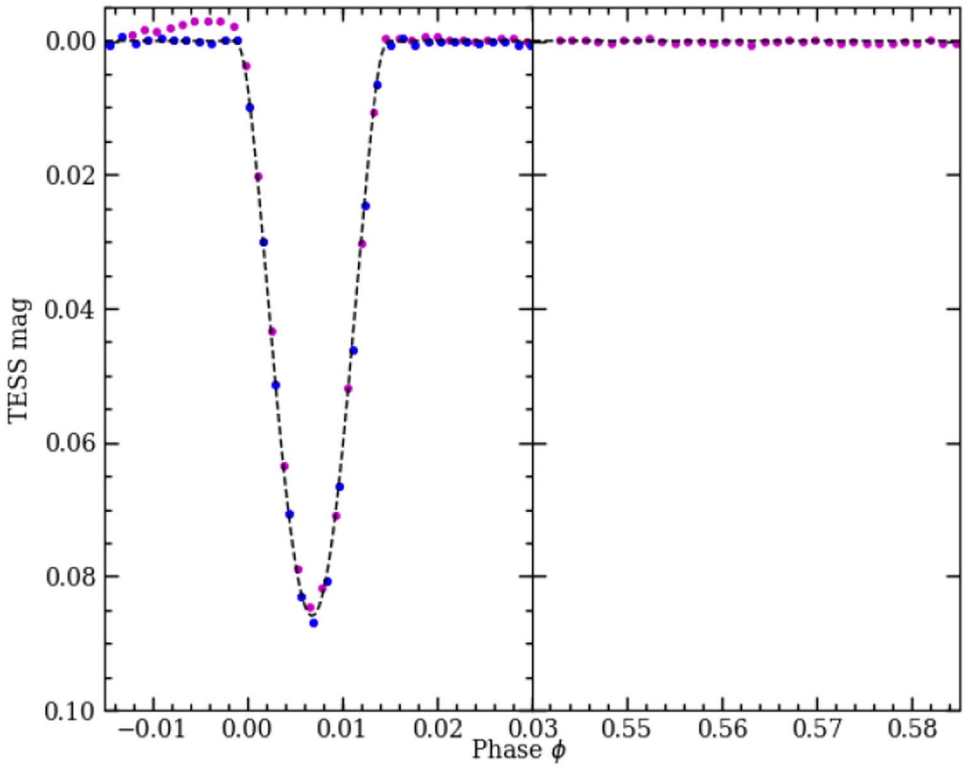

Figure 14. Phased TESS photometry for BD +37 410 compared with the best-fit binary models at the eclipse and noneclipsing conjunction. The first TESS eclipse is shown with magenta points and the second with blue.

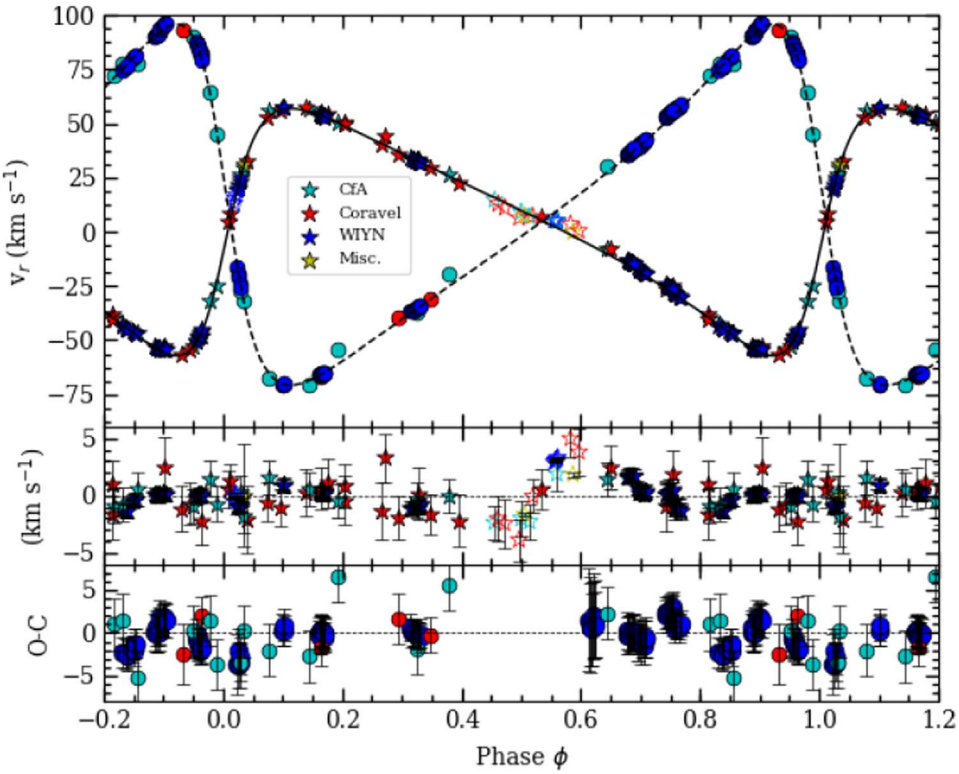

Figure 15. Top panel: radial velocities of the stars in BD +37 410, phased to the orbital period, along with best-fit models. Empty symbols show measurements not used in the orbit fitting. Bottom panels: $(O - C)$ residuals for the radial velocities.

subgiant. Therefore, the *combination* of observed mass, radius, and evolutionary state has the potential to *rule out* isochrone models that do not match.

In Figure 21, we compare the characteristics of the BD +37 410 primary and DS And stars with solar-metallicity isochrones. Metallicity has very little effect on the radii of

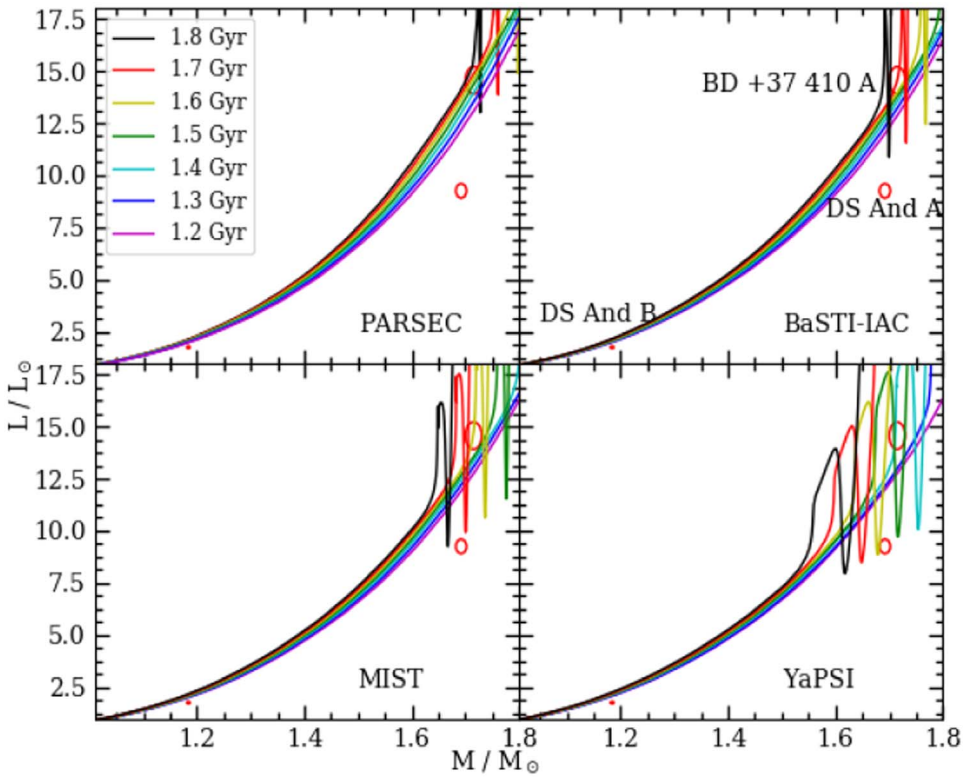

Figure 16. Mass–luminosity plot for measured members of BD +37 410 and DS And, with 2σ uncertainties indicated by the red error ellipses. Models use $Z = 0.0152$, 0.0149, 0.0142, and 0.0162, respectively, for PARSEC (Bressan et al. 2012), BaSTI-IAC (Hidalgo et al. 2018), MIST (Choi et al. 2016; Dotter 2016), and YaPSI (Spada et al. 2017) isochrones.

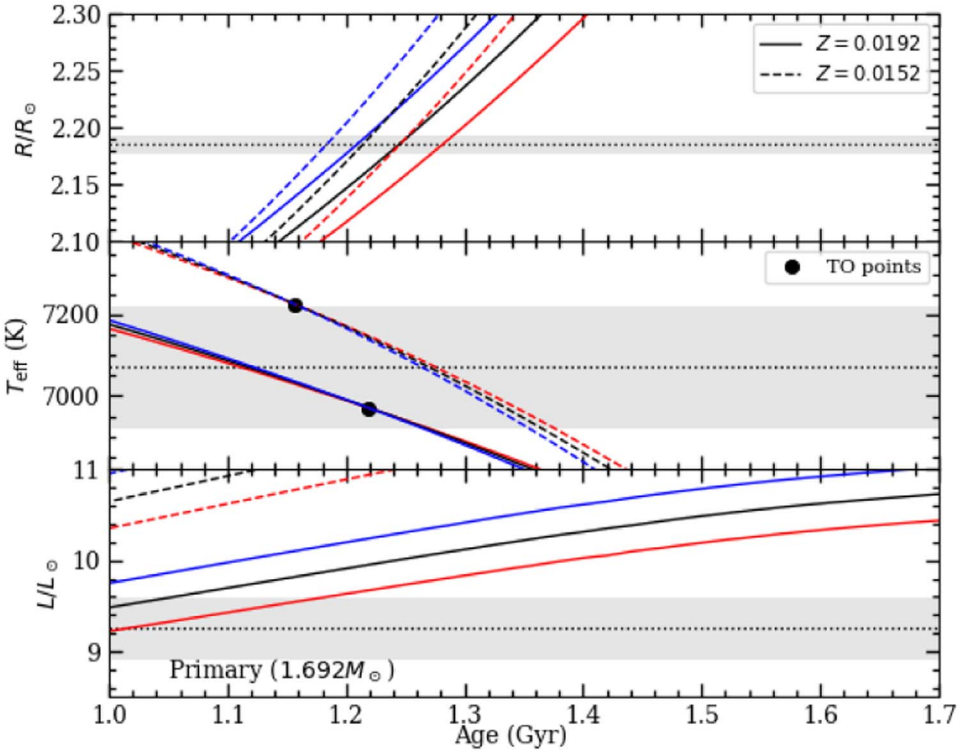

Figure 17. Evolution of model characteristics for DS And A, according to MIST (Choi et al. 2016; Dotter 2016) models for two different metal contents Z. Black lines show evolution tracks for the measured mass, with red and blue lines showing tracks offset in mass by $\pm 1\sigma$. Black dots in the $T_{\rm eff}$ plot show the turnoff value for the corresponding Z. Gray bars show the $\pm 1\sigma$ uncertainty around the measured characteristics of DS And A.

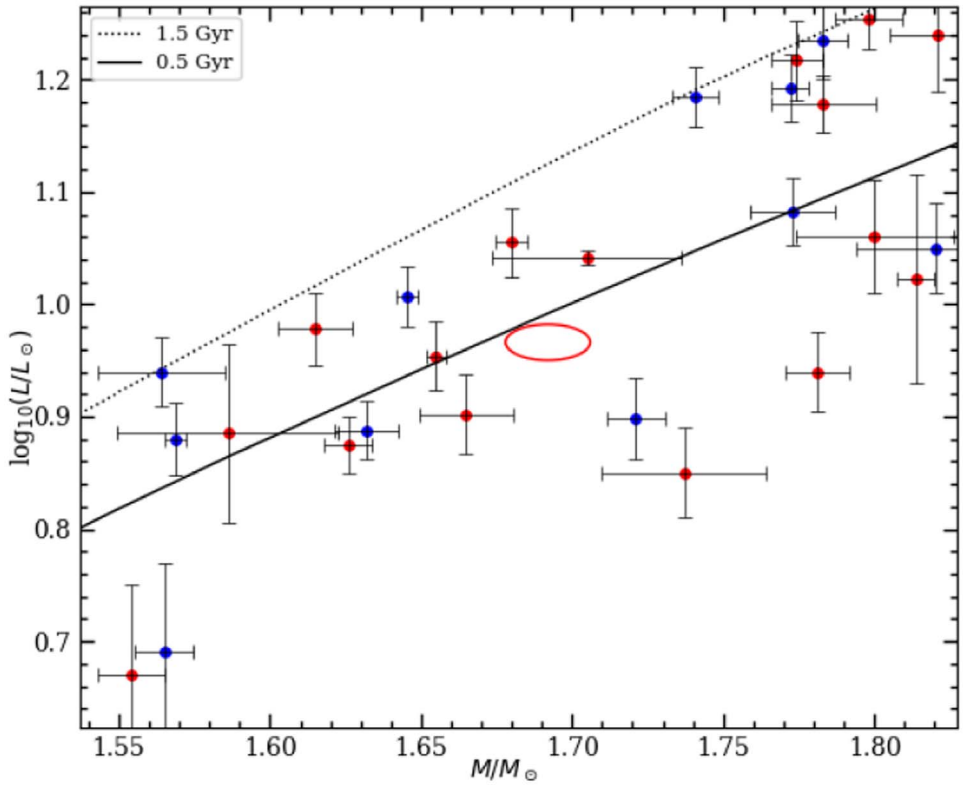

Figure 18. Mass–luminosity plot for measured eclipsing binary stars from the DEBCat database (retrieved 2019; Southworth 2015), with 2σ error bars (showing primary stars in blue and secondary stars in red). The 2σ uncertainties for DS And A are indicated by the red error ellipse. PARSEC (Bressan et al. 2012) isochrones are shown for $Z = 0.0152$.

Table 7
Eclipsing Binary Star Comparisons for DS And A

Star	P (days)	$M/M_\odot$	$R/R_\odot$	$T_{\rm eff}$ (K)	$L/L_\odot$	References
HW CMa A[a,b]	21.118	1.721 ± 0.011	1.643 ± 0.018	7560 ± 150	7.91 ± 0.68	1
AY Cam B	2.735	1.705 ± 0.036	2.025 ± 0.015	7395 ± 100	11.01 ± 0.16	2
DS And A	1.011	1.692 ± 0.004	2.185 ± 0.004	7070 ± 150	9.25 ± 0.34	
EI Cep B[a]	8.439	1.6801 ± 0.0062	2.329 ± 0.044	6950 ± 100	11.35 ± 0.81	3
TV Nor B	8.524	1.665 ± 0.018	1.550 ± 0.014	7800 ± 100	7.98 ± 0.67	4
IO Aqr B	2.368	1.655 ± 0.004	2.493 ± 0.017	6336 ± 125	9.00 ± 0.65	5
V501 Mon A[c]	7.021	1.6455 ± 0.0043	1.888 ± 0.029	7510 ± 100	10.16 ± 0.65	6

Notes.
[a] Am star.
[b] Measured [Fe/H] $= +0.33 \pm 0.15$.
[c] Measured [Fe/H] $= +0.01 \pm 0.06$.
References. (1) Torres et al. (2012), (2) Williamon et al. (2004), (3) Torres et al. (2000), (4) North et al. (1997), (5) Graczyk et al. (2015), (6) Torres et al. (2015), (7) Hoyman et al. (2020).

model stars and is not the cause of the differences between isochrone sets in the figure. Core overshooting primarily affects observable stellar characteristics at core hydrogen exhaustion and afterwards, and smaller amounts of overshooting allow the core to exhaust its core hydrogen supply earlier, before it has a chance to expand as greatly. The very last phase of the main sequence, as the star burns the last few percent of its core hydrogen, shows up as a short downward dip in the mass–radius isochrones. Among the models we plot, the YaPSI models have the least overshooting in the age range we are examining ($\sim 0.1 H_P$ for stellar masses $1.6 M_\odot < M < 1.8 M_\odot$, where H_P is the pressure scale height). The PARSEC models have the largest overshooting ($\sim 0.25 H_P$ for $M > 1.5 M_\odot$). PARSEC (Bressan et al. 2012) and BaSTI-IAC (Hidalgo et al. 2018) model stars reach a radius of $\sim 3 R_\odot$ while on the main sequence, while models with less overshooting only hit that size after starting the subgiant branch. This fact is very important for age determination in NGC 752 because by ruling out models with smaller convective core overshooting it greatly reduces the systematic error associated with uncertainties in the overshooting and allows us to focus on models that realistically match observations. The mass–radius combination for BD +37 410 A points to an age of 1.61 ± 0.03 Gyr. The stellar radii are not very sensitive to metal content, but an increase in metallicity of 0.05 dex (due to observational error or uncertainties in the solar metal content) produces a larger age

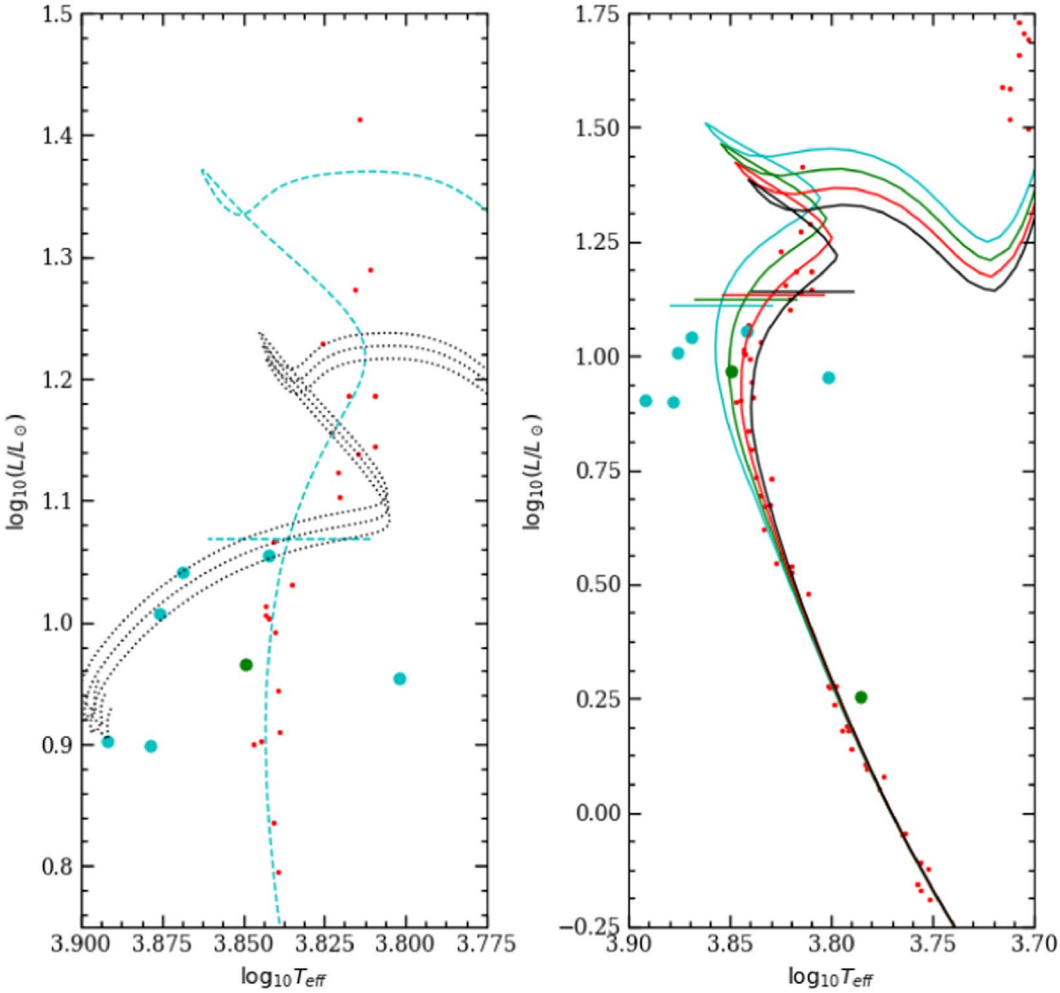

Figure 19. HR diagrams showing NGC 752 single-star candidates (red points), DS And A (green point), and eclipsing binary components of similar mass (cyan points). Left panel: 1.4 Gyr isochrone (cyan dotted line) and a $1.692 \pm 0.01 M_\odot$ evolution tracks (black dotted lines) from the MIST database (Choi et al. 2016; Dotter 2016) for $Z = 0.0152$. Right panel: PARSEC isochrones for $Z = 0.0152$ and ages 1.4 (cyan), 1.5 (green), 1.6 (red), and 1.7 (black) Gyr.

by 0.05 Gyr. We quote this source of uncertainty separately from the statistical uncertainties associated with the fitting of BD +37 410 A's radius.

It is important to emphasize that this conclusion would not have been possible without the mass measurements in particular. Reasonable fits to the CMDs by themselves are possible with all of the isochrone sets we have discussed here. However, the fits with isochrones having smaller amounts of convective overshooting have systematically lower ages. What we are showing here is that the models with the smallest amounts are not consistent with all of the available data, and they must be eliminated from consideration when determining the absolute age of the cluster.

4.3.3. The Stars of DS And, their History, and their Future

Evidence from earlier studies indicated that the characteristics of DS And B have been altered away from that of a normal single star, as it is found well to the red of the main sequence. In Section 3.2.2, we derived characteristics of DS And B star from photometry and the Gaia distance. The temperature analysis indicated that it was approximately 200 K cooler than stars at similar brightness. The mass–radius comparison in Figure 21 appears to confirm that it is larger in size than normal main-sequence stars by a few percent. Together these characteristics appear to make the star less luminous than model predictions by about 10%.

For the primary star, it appears to have a radius similar to other stars at the turnoff, but it is slightly hotter. To summarize the earlier discussion, the luminosity of DS And A appears to be significantly lower than other well-studied eclipsing stars in the field and model predictions for the measured mass, and changes to chemical composition or physics (specifically convective core overshooting) are not capable of explaining the discrepancy. The temperature measured from the SED can be brought into better agreement with models if a higher bulk metallicity is adopted, although this appears to be contrary to what the cluster main sequence implies. The star's radius seems to be the characteristic that is least sensitive to metallicity uncertainties. Models can match the mass and radius of DS And A at the turnoff if core overshooting is at the high end of what is used in models currently ($\sim 0.3 H_P$, with the closest match being PARSEC models), but this does not fix the luminosity discrepancy. The characteristics of DS And A are more precisely determined than those of BD +37 410, and they imply a much lower age: near 1.3 Gyr for PARSEC and BaSTI-IAC isochrones, which are preferred based on convective overshooting arguments. However, we believe that the low age is another symptom of the peculiarities of DS And A. Although

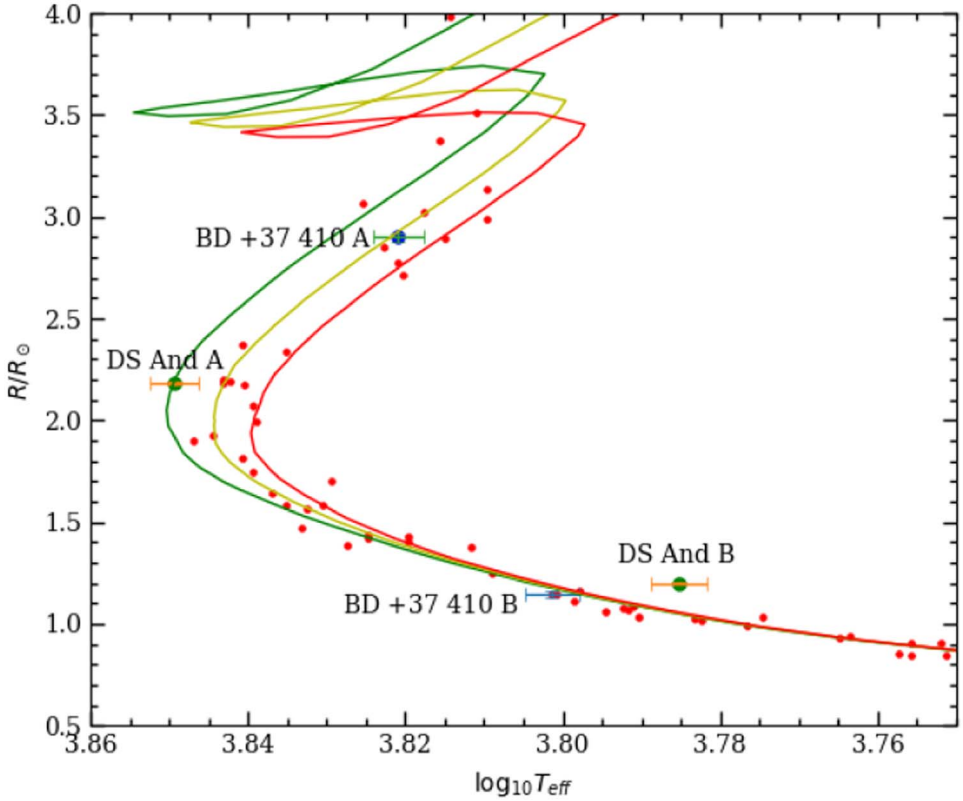

Figure 20. Photometric radii vs. effective temperature for single-star candidates in NGC 752, compared to PARSEC isochrones for 1.5, 1.6, and 1.7 Gyr.

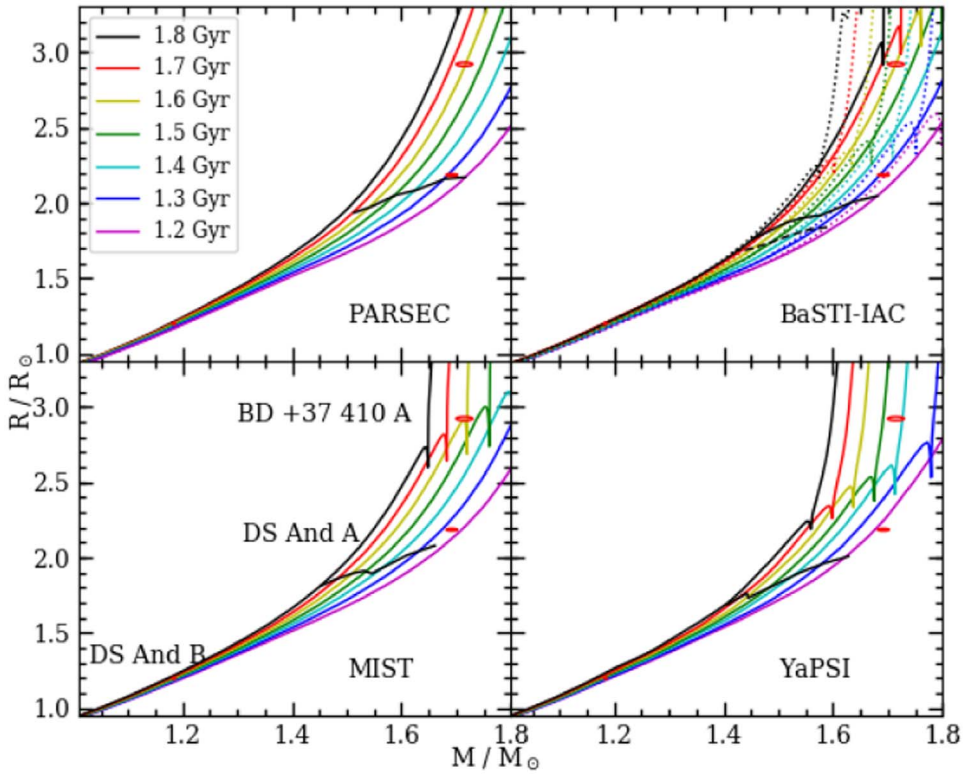

Figure 21. Mass–radius plot for measured members of DS And and BD +37 410 A, with 2σ uncertainties indicated by the red error ellipses. Models use $Z = 0.0152$, 0.0149, 0.0142, and 0.0162, respectively for PARSEC (Bressan et al. 2012), BaSTI-IAC (Hidalgo et al. 2018), MIST (Choi et al. 2016; Dotter 2016), and YaPSI (Spada et al. 2017) isochrones. In the BaSTI-IAC panel, dotted lines show models without convective core overshooting. Solid black lines connect the lower turnoff points on the different isochrones (with the dashed lines in the BaSTI-IAC panel for models without convective core overshooting).

its CMD positions do not disagree wildly with those of other stars at the cluster turnoff, its mass does appear to be noticeably larger than would be expected based on the age derived from BD +37 410. This probably points to it being an emerging blue straggler, and the age implied by the star probably should not be trusted for the cluster.

The future of the DS And binary system is fairly clear, based on its current configuration. The current primary star will evolve and expand to fill its Roche lobe relatively shortly (approximately 200 Myr), while it is still in the late stages of the main sequence. With the relatively slow mass transfer, the secondary star should be able to take in most of the mass of the secondary star without overflowing its Roche lobe, which would be expanding during the transfer. For a time the mass gainer would be a more obvious blue straggler until it evolved off the main sequence and onto the giant branch. Mass transfer at that point is likely to be unstable, leading to a common envelope phase and merger.

Based on the unusual present-day characteristics of the two stars, it is natural to wonder if the stars had an unusual formation history, or were somehow affected by evolving in the presence of another very nearby star. Characteristics of the secondary star might be explained in part by magnetically suppressed convective motions in surface layers. As discussed by Clausen et al. (2009), solar-type stars that are the lower-mass component in close binaries frequently appear to be older than the high-mass component, and there is evidence from X-ray emission that this is related to stellar activity driven by rapid rotation and enforced by tidal interaction. DS And is not the closest binary among systems showing these effects, nor is DS And B the most rapidly rotating of the stars. It is, however, more massive than stars previously identified, and presumably this means that its surface convection zone is significantly smaller in extent and less massive. The evidence may be enough to give it membership in the group, helped by the relatively short period. More examination of activity indicators for this system would be helpful. To date, the tentative detection of the binary in ROSAT PSPC data (a result of being outside the most reliable 20′ of the observed field) by Belloni & Verbunt (1996) remains the only X-ray observation.

DS And A, however, is too massive to have a significant surface convection zone on the main sequence, and so we should look elsewhere for an explanation of its characteristics. The stars of DS And appear to be relaxed and stable in their gravitational potentials, and so it is hard to imagine that the emitted luminosity of the primary could be lower than a star of the same mass would need to maintain its structure as a single star. A zero-age main-sequence star should provide lower limits for both the luminosity and the radius, and we do find that DS And A is above both of these limits for a model star of its mass.

The primary star appears somewhat evolved according to its radius, as if it had a different birth date than other cluster stars. A stellar merger might have resulted in a younger-looking star by bringing hydrogen-rich material into the core. However, if such a thing did occur, it must have happened early in the star's history or otherwise the remnant would not have had a chance to evolve as far away from the zero-age main sequence as it has. Based on the configuration of the binary now, such an event must have involved at least three stars, and would have had to be relatively long ago for the system to have circularized and synchronized. The low luminosity and temperature of the star is not explained in this kind of scenario though. Once a merger remnant relaxed, it should not have been much different than a normal single star—the denser, lower-mass star in a merger would take up a place in the core of the star, giving it a lower core He abundance than a single star of its mass and the cluster's age would have.

A binary mass transfer scenario has more substantial problems. Neither star in the binary appears to have enough mass to have evolved and expanded to reach its Roche lobe to initiate mass transfer. If the secondary star had originally been more massive and had initiated mass transfer in the distant past as a main-sequence star, there is not a clear reason why mass transfer would terminate when the donor was a relatively normal-looking main-sequence star of $1.18 M_{\odot}$.

While Li abundance measurements among bright NGC 752 main-sequence stars are surprisingly few, the stars bracketing DS And A in magnitude (see Figure 10) have the highest abundances (Boesgaard et al. 2022). Although measurement of the Li abundance of DS And A is beyond the scope of this paper, the lack of detectable Li in the primary star's atmosphere is a puzzle. If the star is the remnant of a merger early in the cluster's history, the more massive input star (that contributes the most to the remnant's surface layers) is unlikely to have depleted its photospheric Li greatly by the time of the merger. Even if it originated where the Li dip is seen in the cluster today, depletion probably would not have progressed significantly in a few hundred million years. This leaves the remnant's main-sequence evolution as the most likely site of depletion. Even though DS And A currently resides at the turnoff brighter than the Li dip where standard stellar evolution theory predicts that there should be no Li depletion, observations show that a fraction of stars are depleted and that this fraction increases as age increases (e.g., Deliyannis et al. 2019). For NGC 7789, with age similar to NGC 752, 13% of the stars above the turnoff have Li abundances more than 1 dex away from the maximum for the cluster. The Li depletion appears to correlate with increasing spindown of cluster stars, so the enforced rapid rotation of DS And A within a tidally locked binary might be expected to reduce depletion (Ryan & Deliyannis 1995).

4.4. Color–Magnitude Diagram (CMD) Comparisons and Cluster Age

In light of the possible anomalies in the characteristics of the stars of DS And, it is worth re-examining other age indicators for the cluster. There is a tremendous amount of photometric information available for the stars of NGC 752 that can be employed for age dating the cluster turnoff. Disagreements between models and observations for turnoff and subgiant stars can reveal failings in the model physics, with core convection being a particularly important consideration for stars in this mass range. The extent of core convection has a pivotal role in determining the hydrogen burning lifetime of the stars, and the way in which stars leave the main sequence reveals details of the distribution of hydrogen near the core. We will focus on PARSEC isochrones because of the evidence that the overshooting algorithm they use is the best match for the characteristics of BD +37 410 and other single stars at the bright end of the main sequence.

We re-examined cluster membership based on Gaia Early Data Release 3 proper motions and parallaxes, and available radial-velocity information from Agüeros et al. (2018) and Gaia Data Release 2. We also examined the wider field membership

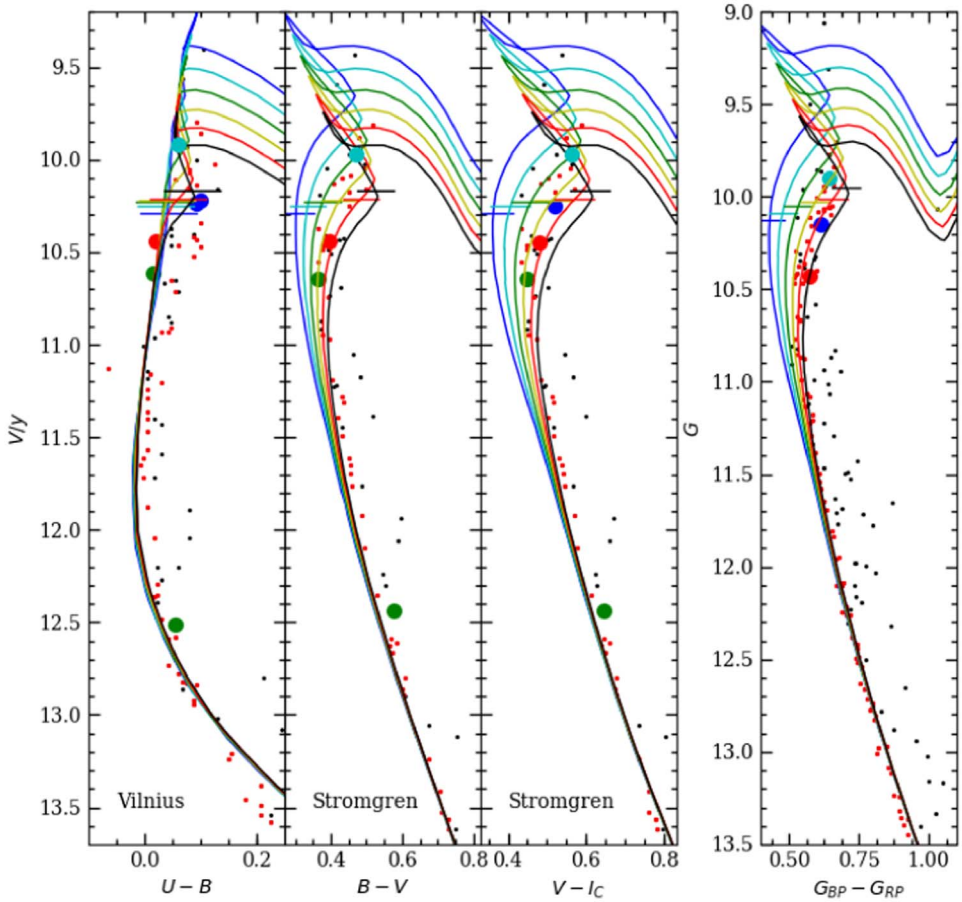

Figure 22. Precise CMDs of likely single-star members of the NGC 752 cluster (small red points) and binary members (black points). Photometry of the DS And system at quadrature is shown with large red points, and the positions of the primary and secondary stars (as inferred from light curves) are shown with green points. Photometry of the BD +37 410 system is shown with cyan points, and a proxy for BD +37 410 A (PLA 641) is shown with blue points. PARSEC isochrones (Bressan et al. 2012) for $Z = 0.0152$ are shown with ages from 1.3 (blue) to 1.8 (black) Gyr with 0.1 Gyr spacing. Horizontal lines mark the position of a star of BD +37 410 A's mass on the isochrone.

searches by Bhattacharya et al. (2021) and Boffin et al. (2022) in the hopes of collecting stars to fill in parts of the main sequence that are sparsely populated. Along the way we noticed an interesting clustering of radial velocities in the 8.5–10 km s^{-1} range, which includes several stars rejected as members by Agüeros et al. (2018) Examining this group of stars, we generally found them to be consistent with membership based on proper motions, parallaxes, and CMD position (frequently being very precisely on the main sequence). We believe the evidence points toward membership for these stars, although we do not have a good explanation for the offset in radial velocity.

We examined CMDs with the most precise photometry. We used Vilnius photometry transformed to Johnson $U - B$ color, and Strömgren photometry transformed to Johnson–Cousins $B - V$ and $V - I_C$ colors; see Section 3.2.1) in order to use high-precision photometry for cluster stars while making use of our photometric decomposition of $UBVR_CI_C$ for the DS And system using light curves. We show these CMDs, along with the Gaia EDR3 CMD in Figure 22. While the ($U - B$, V) data and models disagree in several complex ways, the agreement is much better in other colors, and isochrone fits purely to the CMDs imply an age of 1.6–1.7 Gyr. But beyond this, the models predictions are in good agreement with the measured photometry of the primary star within the uncertainties on its measured mass.

With the variety of photometry available for NGC 752 stars, we assembled an HR diagram for stars near the turnoff using SED fits and Gaia distance information. We have generally restricted our sample to stars that have at least one measurement in U or similar filters shortward of the Balmer decrement in order to gauge gravity effects on the SED. The HR diagram is most consistent with solar metallicity—if a higher metallicity is used, the main sequence is predicted to be too red. The other factor that must be constrained is the amount of convective core overshooting. Redward extension of stars brighter than the turnoff is sensitive to the amount, with more overshooting prolonging the slow phase of core hydrogen burning and allowing the stars to grow bigger and more luminous before reaching core hydrogen exhaustion. As shown in Section 4.3.2, the brightest turnoff stars support the larger amount of overshooting in the PARSEC models over the other isochrone sets. Thus, our preferred age for NGC 752 is near 1.6 Gyr, with an uncertainty of about 0.08 Gyr that comes from the scatter in the stars in the brightest main sequence.

We can derive ages relative to other clusters by selecting high-probability members based on Gaia proper motions and parallaxes, and using the parallaxes for distance corrections. Based on the apparent age of NGC 752, a good comparison is NGC 6811, with an age close to 1 Gyr (Sandquist et al. 2016). NGC 6811 is close enough that parallaxes have also been measured for main-sequence stars far below the turnoff.

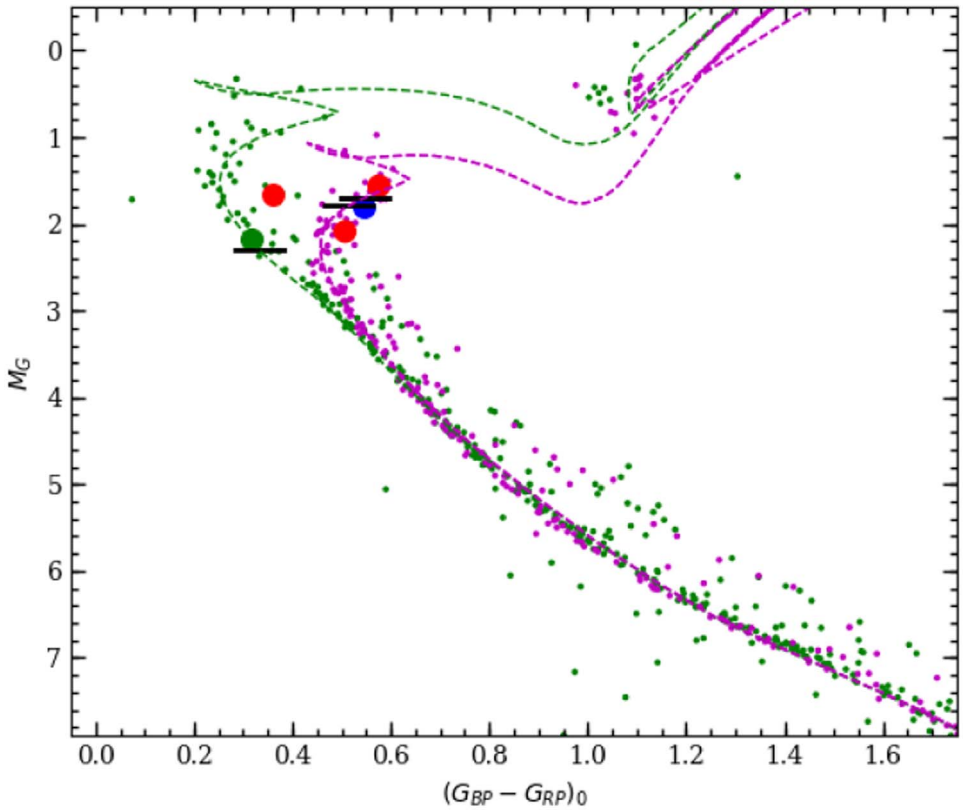

Figure 23. Color–magnitude diagram for NGC 752 (magenta points) and NGC 6811 (green) cluster members selected based on Gaia proper motions and parallaxes from Early Data Release 3. PARSEC isochrones for $Z = 0.0152$ and ages 1.00 and 1.60 Gyr are shown. The black marks shows where stars with the mass of KIC 9777062 A, DS And A, and BD +37 410 A would be in the respective isochrones. The large red points show the mean photometry for all three binaries, the large green point shows the approximate characteristics of KIC 9777062 A, and the blue point shows the characteristics of a proxy for BD +37 410 A.

Figure 23 shows a comparison between likely members of the two clusters where the photometry was corrected for the Gaia mean cluster parallaxes (2.24 mas and 0.87 mas for NGC 752 and NGC 6811, respectively) and for extinction ($E(B-V) = 0.044$ and 0.07, respectively) using the prescription in Gaia Collaboration et al. (2018). The main sequences of the two clusters overlap each other extremely well except near the turnoff, clearly showing that NGC 752 is older. Using PARSEC models (Bressan et al. 2012), we estimate that the two clusters differ in age by about 0.6 Gyr.

The age that we prefer is larger than all recent measurements, and in some cases, significantly so. An important factor in the discussion is the amount of convective core overshooting because the size of the mixed core during the main-sequence phase affects the duration of core hydrogen burning while leaving most other observable characteristics nearly unchanged. So unless the overshooting in the models is calibrated, there could be a substantial systematic error. We briefly discuss recent age measurements below.

Bartašiūtė et al. (2007) derived an age of 1.58 ± 0.04 Gyr, using Padova isochrones (Bressan et al. 1993) to do a least-squares fit to Vilnius photometry for the cluster. Their procedure selected a model metallicity ($Z = 0.015$) close to what we use, but the distance modulus ($(m-M)_V = 8.18 \pm 0.03$) is somewhat smaller than implied by Gaia measurements. While their measurement is consistent with ours, Padova isochrones have larger overshooting ($\sim 0.5 H_P$) than the successor PARSEC isochrones for stars in this mass range, but this is not likely to have affected their fits to main-sequence stars a great deal.

Twarog et al. (2015) found an age of 1.45 ± 0.05 Gyr using Victoria–Regina isochrones (VandenBerg et al. 2006) in their analysis of Strömgren photometry. The Victoria–Regina isochrones have similar amounts of overshooting as PARSEC isochrones despite a different algorithm. The solar metal content used in the Victoria–Regina models ($Z_\odot = 0.0188$) is quite a bit larger than the PARSEC models ($Z_\odot = 0.0152$), although it is closer to the one recent re-examination of the solar metal content by Magg et al. (2022). Their best-fit models used [Fe/H] $= -0.04$ or $Z = 0.0171$, so they had a larger metal content than the models we used. If the model composition differences are taken into account, our estimations would probably be quite close. But this comparison emphasizes that uncertainties in the bulk metal content of the stars remains an important systematic.

Although Gaia Collaboration et al. (2018) did not do a detailed exploration of parameter space, they were the first to make use of Gaia photometry and distance information, alongside representative metallicity ([Fe/H] $= -0.03$) and reddening ($E(B-V) = 0.04$) values. The authors derived an age of 1.4 Gyr using PARSEC isochrones, which we believe have an appropriate amount of convective overshooting, but they do also quote a fairly large uncertainty of more than 0.2 Gyr.

Agüeros et al. (2018) derived an age of 1.34 ± 0.06 Gyr for NGC 752 through photometric SED fits to 59 of the most likely single stars in their membership survey. The cluster parameters were derived from the combination of the individual posterior distributions for the single-star sample. While this is a statistically thorough age determination, it is still subject to systematics. For example, their analysis only employed MIST isochrones, which

have an amount of overshooting that is too small to match the characteristics of the brightest main-sequence stars. Only a portion of their sample had much leverage on the age, as evidenced in their Figure 3 by a number of stars that returned zero ages or ages two or more times the likely age. In addition, their result for the cluster extinction A_V was at the high end of the prior range they searched, and is larger than found in other studies. This may be a reflection of systematic error as well.

5. Conclusions

An analysis of the eclipsing binary BD +37 410 reveals a primary star that has evolved past the cluster turnoff nearing the end of the heavily populated part of the main sequence in NGC 752, and its characteristics clearly show the consequences of strong convective overshooting in the star's core that prolong the main-sequence lifetime. The luminosity and radius of the star are inconsistent with predictions from some commonly used sets of isochrones, and as a result this observation greatly reduces systematic errors in the cluster's age associated with convective core overshooting. Overshooting algorithms are the subject of continuing research, and they are almost certain to be imperfectly representing the behavior of the convective core as a function of time in stars such as those at the turnoff of NGC 752. But in terms of reproducing the extent of core convection shortly before core hydrogen exhaustion, PARSEC models are clearly coming closest. Based on CMD comparisons and especially the mass and radius of the primary star of BD +37 410, our preferred age is $1.61 \pm 0.03 \pm 0.05$ Gyr.

We have also presented measurements of the close eclipsing binary system DS And, which contains a star near the turnoff of the nearby open cluster NGC 752. We have improved the precision and accuracy of the radial-velocity measurements for the binary, which lead to precise masses $M_1 = 1.692 \pm 0.004 \pm 0.010 M_\odot$ and $M_2 = 1.184 \pm 0.001 \pm 0.003 M_\odot$. Light curves in nine different wavelength bands allow us to separate the contributions to the system light from the two stars and to derive effective temperatures. Analysis of the eclipsing light curves allows us to derive precise radii $R_1 = 2.185 \pm 0.004 \pm 0.008 R_\odot$ and $R_2 = 1.200 \pm 0.003 \pm 0.005 R_\odot$. The stars are in a very close binary, although they are pretty clearly detached, with a few percent distortion of the shape of the primary star. The stars rotate significantly faster than stars of similar brightness in the cluster: $v_{\rm rot} \sin i = 105, 58$ km s^{-1}, while likely single stars in the cluster generally have $v_{\rm rot} < 35$ km s^{-1} (Mermilliod et al. 2009). A relatively high amount of convective core overshooting appears to be needed to match its radius at its evolutionary stage at the turnoff. The star's temperature is in line with other stars at the turnoff, and the star's radius is clearly lower than expected when we compare to the primary star of BD +37 410. The star's luminosity is also significantly lower than predicted for reasonable models. We do not have a clear explanation for all of the primary star's characteristics, but a stellar merger early in the cluster's history is consistent with the most data.

Together, both binary systems clearly show that stars with mass near $1.7 M_\odot$ inhabit NGC 752's turnoff and are in the last stages of main-sequence evolution. The best-fitting models predict that stars with masses of 1.77–$1.80 M_\odot$ are leaving the main sequence. This is important to know because of the well-known fact that NGC 752 is one of the few star clusters known with red clump stars covering a large range of magnitudes, indicating its most massive stars are making the transition from nondegenerate helium ignition (which happens at relatively low He core mass, and results in lower-luminosity clump stars) to degenerate He flash ignition. While a detailed analysis of the clump stars is beyond our scope here, the mass information should be very valuable in further examination of the physics governing the giant branch and helium ignition at this transition.

E.L.S. gratefully acknowledges support from the National Science Foundation under grant AAG 1817217. We thank the anonymous referee for a thorough reading of the manuscript and for many helpful comments on presentation. We thank K. Brogaard for providing the original version of the spectral disentangling code used in this work, B. Twarog for providing his Strömgren photometry of DS And, and H. Boffin for providing the results of his membership study for NGC 752. We would also like to thank D. Baer, E. Bavarsad, D. Jaimes, and M. J. Jeffries, Jr. for assisting in the acquisition of ground-based photometric observations.

This research made use of observations from the SIMBAD database, operated at CDS, Strasbourg, France; and the WEBDA database, operated at the Institute for Astronomy of the University of Vienna; data products from the AAVSO Photometric All Sky Survey (APASS), funded by the Robert Martin Ayers Sciences Fund and the National Science Foundation. The Hobby–Eberly Telescope (HET) is a joint project of the University of Texas at Austin, the Pennsylvania State University, Stanford University, Ludwig-Maximilians-Universität München, and Georg-August-Universität Göttingen. The HET is named in honor of its principal benefactors, William P. Hobby and Robert E. Eberly.

Facilities: MLO:1 m, HET (HRS), NOT (FIES), WIYN (Hydra), TESS.

Software: IRAF (Tody 1986, 1993), DAOPHOT (Stetson 1987), ELC (Orosz & Hauschildt 2000), eleanor (Feinstein et al. 2019), FIEStool (http://www.not.iac.es/instruments/fies/fiestool/FIEStool.html), QLP (Huang et al. 2020), BF-rvplotter (https://github.com/mrawls/BF-rvplotter).

Appendix
Photometry Sources and Spectral Energy Distribution Fitting

Table 8 holds information on the photometry we used to delineate the SEDs of NGC 752 stars. We provide references for the photometry and for the calibration to flux. Table 10 provides the system fluxes for the two binaries in this study.

The GALEX observations of the cluster involved guest investigator images in the far-ultraviolet (FUV) for 4539 s (GI1 proposal 27, P.I. K. Honeycutt), and near-ultraviolet (NUV) exposures as part of the All-Sky Imaging Survey (AIS). Archived magnitudes are based on count rates with minimal background contributions, so we computed the magnitude and flux based on the average count rate for redundant AIS observations in the NUV. Morrissey et al. (2007) describes the characteristics of the GALEX photometry and its calibration to flux.

We fitted the photometric data for $T_{\rm eff}$ and bolometric flux $F_{\rm bol}$ using ATLAS9 models (Castelli & Kurucz 2003).[16] Models were adjusted to account for the interstellar reddening

[16] The models were calculated using the ATLAS9 Fortran code that employed updated 2015 line lists, and we computed models at finer temperature intervals than are available in the published grid.

Table 8
Sources of Photometry for NGC 752 Spectral Energy Distributions

Facility/Survey	Filter	$\lambda_{\rm eff}$ (Å)	References	Calibration	Notes
GALEX	FUV	1538.6	Martin et al. (2005)	Morrissey et al. (2007)	
	NUV	2315.7			
Swift-UVOT	*uvw*2	2030	Siegel et al. (2019)		
	*uvm*2	2231			
	*uvw*1	2634			
XMM-Newton	*uvw*1	2971			1
Vilnius	U_V	3450	Bartašiūtė et al. (2007)	Mann & von Braun (2015)	
	P_V	3740	Zdanavičius et al. (2010)		
	X_V	4054			
	Y_V	4665			
	Z_V	5162			
	V_V	5442			
	S_V	6534			
Strömgren	u	3520	Twarog et al. (2015)	Gray (1998)	
	v	4100	Hauck & Mermilliod (1998)		
	b	4688			
	y	5480			
Geneva	U_G	3471	Rufener (1988)		2
	$B1_G$	4023			
	B_G	4246			
	$B2_G$	4482			
	$V1_G$	5402			
	V_G	5504			
	G_G	5814			
UBV Means	U	3663	Mermilliod & Mermilliod (1994)	Bessell et al. (1998)	3
	B	4361			
	V	5448			
Tycho	B_T	4220	Høg et al. (2000)	Mann & von Braun (2015)	6
	V_T	5350			
D94	B	4361	Daniel et al. (1994)	Bessell et al. (1998)	3
	V	5448			
APASS	B	4361	Henden et al. (2015)	Bessell et al. (1998)	3,9
	V	5448			
	g'	4640			
	r'	6122			
	i'	7440			
Pan-STARRS1	g_{P1}	4810	Kaiser et al. (2010)	Schlafly et al. (2012)	5
	r_{P1}	6170			
	i_{P1}	7520			
	z_{P1}	8660			
	y_{P1}	9620			
T08	V	5448	Taylor et al. (2008)	Bessell et al. (1998)	3
	R_C	6414			
	I_C	7980			
TASS	V	5448	Droege et al. (2006)	Bessell et al. (1998)	3,4
	I_C	7980			
Gaia	G_{BP}	5051.5			7
	G	6230.6			
	G_{RP}	7726.2			
2MASS	J	12350	Skrutskie et al. (2006)	Cohen et al. (2003)	8
	H	16620			
	K_s	21590			
WISE	W1	33526	Wright et al. (2010)		
	W2	46028			
	W3	115608			

Note. (1) XMM-Newton Optical Monitor Serendipitous Source Catalogue (Version 4.1). (2) Retrieved from WEBDA. (3) Measurements on a Vega magnitude system, converted to fluxes using reference magnitudes from Table A2 of Bessell et al. (1998), accounting for the reversal of the zero-point correction rows for f_λ and f_ν. (4) The Amateur Sky Survey Mark IV catalog version 2. (5) Mean point-spread function magnitudes used. (6) Tycho-2 Catalogue. (7) Early Data Release 3. (8) Photometry from the All-Sky Point Source Catalog. (9) Data Release 10.

of the cluster ($E(B-V) = 0.044 \pm 0.0034$; Taylor 2007) using the Cardelli et al. (1989) extinction curve. We commonly have flux information from the ultraviolet into the infrared, so that $T_{\rm eff}$ is delimited well. However, we employed the infrared flux method (IRFM; Blackwell & Shallis 1977) to get better precision on the temperature. The ratio of bolometric and

Table 9
Radial-velocity Measurements

mJD[a]	v_A (km s^{-1})	σ_A	v_B (km s^{-1})	σ_B	v_C (km s^{-1})	σ_C
			DS And			
			NOT FIES Observations			
54,335.55788	125.15	1.18	−167.19	1.03		
54,336.53919	125.54	1.20	−172.07	1.78		
54,336.60635	117.35	1.30	−152.54	1.12		
54,336.75052	44.80	1.31	−60.97	1.99		
54,337.49382	118.94	1.11	−159.96	1.14		
54,337.56653	127.33	1.47	−170.93	1.18		
54,671.59838	−105.79	0.90	166.21	1.64		
54,671.62437	−96.08	0.63	148.69	1.31		
54,671.67465	−68.85	0.73	109.15	1.05		
54,693.60647	−67.93	0.86	101.64	0.65		
54,696.64674	−72.44	0.54	114.02	1.12		
54,707.53952	87.36	0.89	−104.93	1.36		
54,762.43073	−112.28	0.71	176.64	0.49		
54,762.49913	−114.01	1.03	181.60	1.27		
54,787.63134	−90.00	0.75	143.26	1.30		
			HET HRS Observations			
55,420.87490	126.50	1.18	−162.40	1.80		
55,421.86256	128.09	0.98	−169.50	1.31		
55,466.98209	−57.56	2.05	95.77	2.36		
55,466.98701	−51.80	2.28	92.64	1.45		
55,470.73432	−88.30	1.35	132.36	0.50		
55,476.94538	−115.92	1.40	178.68	1.55		
55,478.94247	−118.67	1.33	182.22	2.54		
55,479.92220	−116.22	1.24	180.50	2.59		
55,486.92143	−98.73	1.25	143.91	1.66		
55,493.89688[b]	−42.86	1.56	82.95	0.65		
55,505.87386	73.52	0.65	−88.84	1.30		

Notes.
[a] mJD = BJD − 2,400,000.
[b] Not used in fit.

(This table is available in its entirety in machine-readable form.)

infrared fluxes (in 2MASS bands) can be compared with an approximate ATLAS9 model to compute a new estimate of $T_{\rm eff}$. We calculated $T_{\rm eff}$ values from all three 2MASS bandpasses, and we used the average as the most representative value. We used the 2MASS flux calibration of Casagrande et al. (2010) because it produced better consistency between the temperatures from the three bands than did the Cohen et al. (2003) calibration. A new ATLAS9 model was computed using the updated $T_{\rm eff}$ and the process was iterated until $T_{\rm eff}$ in the model and $T_{\rm eff}$ from the IRFM agreed.

For cluster single stars, we generally only fitted stars with at least one measurement in U or similar bandpasses in order to monitor whether the gravity-sensitive Balmer decrement feature was being modeled properly. Trends in the flux residuals ($\Delta F_\lambda/F_\lambda$) as a function of wavelength were monitored to ensure that there were not gross errors in the

Table 10
Photometry of DS And and BD +37 410

Filter	$\lambda_{\rm eff}$ (Å)	m_λ	σ_m	F_λ (erg cm^{-2} s Å)	m_λ	σ_m	F_λ (erg cm^{-2} s Å)	Notes
FUV	1538.6	18.394	0.0137	2.073×10^{-15}	19.0833	0.0209	1.099×10^{-15}	
NUV	2315.7	14.599	0.0079	3.208×10^{-14}	14.2347	0.0014	4.487×10^{-14}	
U_V	3450	12.704		1.554×10^{-13}	12.260		2.339×10^{-13}	2
U_G	3471				10.955		2.388×10^{-13}	10
u	3520	12.245	0.022	1.482×10^{-13}	11.711	0.004	2.424×10^{-13}	1
U	3663	10.852	0.005	1.905×10^{-13}				7
U	3663	10.915	0.009	1.798×10^{-13}	10.473	0.004	2.701×10^{-13}	4
P_V	3740	12.177		1.925×10^{-13}	11.71		2.960×10^{-13}	8,2
$B1_G$	4023				10.584		3.948×10^{-13}	10
X_V	4054	11.541		2.728×10^{-13}	11.09		4.133×10^{-13}	8,2
v	4100	11.210	0.018	2.841×10^{-13}	10.705	0.005	4.524×10^{-13}	1
B_T	4220	11.140	0.052	2.379×10^{-13}	10.431	0.035	4.571×10^{-13}	
B_G	4246				9.583		4.234×10^{-13}	10
B	4361	10.833	0.009	2.935×10^{-13}				7
B	4361	10.913	0.003	2.726×10^{-13}	10.438	0.001	4.223×10^{-13}	5
B	4361	10.89		2.785×10^{-13}	10.435	0.004	4.234×10^{-13}	4
B	4361	10.862	0.061	2.858×10^{-13}	10.517	0.182	3.926×10^{-13}	3
$B2_G$	4482				10.952		4.512×10^{-13}	10
Y_V	4665	10.922		2.905×10^{-13}	10.44		4.529×10^{-13}	2
g'	4640	10.650	0.062	2.775×10^{-13}	10.355	0.133	3.640×10^{-13}	3
b	4688	10.770	0.012	2.898×10^{-13}	10.255	0.003	4.657×10^{-13}	1
g_{P1}	4810				10.038	0.010	4.537×10^{-13}	
G_{BP}	5051.5	10.7285	0.0396	2.120×10^{-13}	10.0748	0.0029	3.871×10^{-13}	
Z_V	5162	10.668		2.477×10^{-13}	10.12		4.103×10^{-13}	8,2
V_T	5350	10.625	0.048	2.266×10^{-13}	9.898	0.031	4.426×10^{-13}	
$V1_G$	5402				10.700		3.916×10^{-13}	10
V_V	5442	10.504		2.371×10^{-13}	9.95		3.950×10^{-13}	8,2
V	5448	10.439	0.004	2.423×10^{-13}	9.967	0.047	3.743×10^{-13}	7,9
V	5448	10.506	0.037	2.278×10^{-13}	9.968	0.013	3.739×10^{-13}	5
V	5448	10.480	0.017	2.333×10^{-13}	9.963	0.030	3.757×10^{-13}	4
V	5448	10.439	0.061	2.423×10^{-13}	10.036	0.003	3.512×10^{-13}	3
y	5480	10.510	0.010	2.332×10^{-13}	9.944	0.003	3.927×10^{-13}	1
V_G	5504				9.963		3.865×10^{-13}	10
G_G	5814				11.037		3.651×10^{-13}	10
r'	6122	10.404	0.070	1.999×10^{-13}				3
r_{P1}	6170				9.836	0.010	3.321×10^{-13}	
R_C	6414	10.222	0.005	1.775×10^{-13}				7
G	6230.6	10.4555	0.0088	1.671×10^{-13}	9.9012	0.0031	2.784×10^{-13}	
S_V	6534	10.084		1.724×10^{-13}	9.48		3.008×10^{-13}	8,2
i'	7440	10.341	0.058	1.435×10^{-13}				3
i_{P1}	7520				9.786	0.079	2.341×10^{-13}	
G_{RP}	7726.2	10.1141	0.0285	1.183×10^{-13}	9.4316	0.0039	2.218×10^{-13}	
I_C	7980	9.959	0.012	1.169×10^{-13}	9.407	0.066	1.944×10^{-13}	7,9
z_{P1}	8660				9.784	0.010	1.769×10^{-13}	
y_{P1}	9620				9.784	0.010	1.433×10^{-13}	
J	12350	9.653	0.018	4.307×10^{-14}	9.001	0.023	7.852×10^{-14}	
H	16620	9.481	0.019	1.827×10^{-14}	8.792	0.018	3.447×10^{-14}	
K_s	21590	9.407	0.014	7.395×10^{-15}	8.696	0.017	1.423×10^{-14}	
W1	33526	9.352	0.023	1.486×10^{-15}	8.695	0.023	2.721×10^{-15}	6
W2	46028	9.368	0.019	4.322×10^{-16}	8.724	0.021	7.822×10^{-16}	6
W3	115608	9.383	0.031	1.150×10^{-17}	8.720	0.022	2.118×10^{-17}	

References. (1) Twarog et al. (2015), (2) Zdanavičius et al. (2010), (3) APASS (v. 10), (4) Mermilliod & Mermilliod (1994), (5) Daniel et al. (1994), (6) Chen et al. (2018) measurement at light-curve maximum, (7) Milone et al. (2019) measurement at light-curve maximum, (8) Bartašiūtė et al. (2007), (9) Droege et al. (2006), (10) Rufener (1988).

temperatures. Clearly discrepant photometric values were removed before the fits were complete.

ORCID iDs

Eric L. Sandquist https://orcid.org/0000-0003-4070-4881
Andrew J. Buckner https://orcid.org/0000-0002-6998-2327
Matthew D. Shetrone https://orcid.org/0000-0003-0509-2656
Catherine A. Pilachowski https://orcid.org/0000-0002-3007-206X
Constantine P. Deliyannis https://orcid.org/0000-0002-3854-050X
Robert Mathieu https://orcid.org/0000-0002-7130-2757
Jerome A. Orosz https://orcid.org/0000-0001-9647-2886

References

Agüeros, M. A., Bowsher, E. C., Bochanski, J. J., et al. 2018, ApJ, 862, 33
Alksnis, A. 1961, PZ, 13, 300
Amby Ottosen, T. 2011, MSc thesis, Aarhus Univ.
Asplund, M., Amarsi, A. M., & Grevesse, N. 2021, A&A, 653, A141
Asplund, M., Grevesse, N., & Sauval, A. J. 2005, in ASP Conf. Ser. 336, Cosmic Abundances as Records of Stellar Evolution and Nucleosynthesis, ed. Thomas G. Barnes, III & Frank N. Bash (San Francisco, CA: APS), 25
Asplund, M., Grevesse, N., Sauval, A. J., & Scott, P. 2009, ARA&A, 47, 481
Bailer-Jones, C. A. L., Rybizki, J., Fouesneau, M., et al. 2021, AJ, 161, 147
Baranne, A., Mayor, M., & Poncet, J. L. 1979, VA, 23, 279
Barnes, S. A. 2007, ApJ, 669, 1167
Bartašiūtė, S., Deveikis, V., Straižys, V., & Bogdanovičius, A. 2007, BaltA, 16, 199
Belloni, T., & Verbunt, F. 1996, A&A, 305, 806
Bessell, M. S., Castelli, F., & Plez, B. 1998, A&A, 333, 231
Bhattacharya, S., Agarwal, M., Rao, K. K., et al. 2021, MNRAS, 505, 1607
Blackwell, D. E., & Shallis, M. J. 1977, MNRAS, 180, 177
Böcek Topcu, G., Afşar, M., Schaeuble, M., & Sneden, C. 2015, MNRAS, 446, 3562
Böcek Topcu, G., Afşar, M., Sneden, C., et al. 2020, MNRAS, 491, 544
Boesgaard, A. M., Lum, M. G., Chontos, A., et al. 2022, ApJ, 927, 118
Boffin, H. M. J., Jerabkova, T., Beccari, G., et al. 2022, MNRAS, 514, 3579
Breger, M. 1968, PASP, 80, 417
Breger, M. 1969, ApL, 3, 67
Bressan, A., Fagotto, F., Bertelli, G., et al. 1993, A&AS, 100, 647
Bressan, A., Marigo, P., Girardi, L., et al. 2012, MNRAS, 427, 127
Butters, O. W., West, R. G., Anderson, D. R., et al. 2010, A&A, 520, L10
Caffau, E., Ludwig, H.-G., Steffen, M., Freytag, B., & Bonifacio, P. 2011, SoPh, 268, 255
Cantat-Gaudin, T., Jordi, C., Vallenari, A., et al. 2018, A&A, 618, A93
Cardelli, J. A., Clayton, G. C., & Mathis, J. S. 1989, ApJ, 345, 245
Carrera, R., & Pancino, E. 2011, A&A, 535, A30
Casagrande, L., Ramírez, I., Meléndez, J., et al. 2010, A&A, 512, A54
Castelli, F., & Kurucz, R. L. 2003, in IAU Symp. 210, Modelling of Stellar Atmospheres, ed. N. Piskunov, W. W. Weiss, & D. F. Gray, (Cambridge: Cambridge Univ. Press), A20
Chen, X., Wang, S., Deng, L., et al. 2018, ApJS, 237, 28
Choi, J., Dotter, A., Conroy, C., et al. 2016, ApJ, 823, 102
Claret, A. 2018, A&A, 618 A20
Claret, A., Hauschildt, P. H., & Witte, S. 2013, A&A, 552, A16
Clausen, J. V., Bruntt, H., Claret, A., et al. 2009, A&A, 502, 253
Coelho, P., Barbuy, B., Meléndez, J., Schiavon, R. P., & Castilho, B. V. 2005, A&A, 443, 735
Cohen, M., Wheaton, W. A., & Megeath, S. T. 2003, AJ, 126, 1090
Cousins, A. W. J. 1987, MNSSJ, 46, 144
Daniel, S. A., Latham, D. W., Mathieu, R. D., et al. 1994, PASP, 106, 281
Deliyannis, C. P., Anthony-Twarog, B. J., Lee-Brown, D. B., et al. 2019, AJ, 158, 163
Dotter, A. 2016, ApJS, 222, 8
Droege, T. F., Richmond, M. W., Sallman, M. P., et al. 2006, PASP, 118, 1666
Feinstein, A. D., Montet, B. T., Foreman-Mackey, D., et al. 2019, PASP, 131, 094502
Forbes, M. C. 1996, PhD thesis, Victoria Univ. Wellington, New Zealand, https://core.ac.uk/download/pdf/41335971.pdf
Francic, S. P. 1989, AJ, 98, 888
Friel, E. D., Liu, T., & Janes, K. A. 1989, PASP, 101, 1105
Gaia Collaboration, Babusiaux, C., van Leeuwen, F., et al. 2018, A&A, 616, A10
Garrison, R. F. 1972, ApJ, 177, 653
Girardi, L., Mermilliod, J.-C., & Carraro, G. 2000, A&A, 354, 892
González, J. F., & Levato, H. 2006, A&A, 448, 283
Graczyk, D., Maxted, P. F. L., Pietrzyński, G., et al. 2015, A&A, 581, A106
Gray, R. O. 1998, AJ, 116, 482
Guo, X., Johnson, J. A., Mann, A. W., et al. 2017, ApJ, 838, 25
Harmanec, P., & Božić, H. 2001, A&A, 369, 1140
Hauck, B., & Mermilliod, M. 1998, A&AS, 129, 431
Henden, A. A., Levine, S., Terrell, D., et al. 2015, AAS Meeting Abstracts, 225, 336.16
Hidalgo, S. L., Pietrinferni, A., Cassisi, S., et al. 2018, ApJ, 856, 125
Hobbs, L. M., & Thorburn, J. A. 1992, AJ, 104, 669
Høg, E., Fabricius, C., Makarov, V. V., et al. 2000, A&A, 355, L27
Honeycutt, R. K. 1992, PASP, 104, 435
Hoyman, B., Çakırlí, Ö., & Özdarcan, O. 2020, MNRAS, 491, 5980
Huang, C. X., Vanderburg, A., Pál, A., et al. 2020, RNAAS, 4, 204
Kaiser, N., Burgett, W., Chambers, K., et al. 2010, Proc. SPIE, 7733, 77330E
Kipping, D. M. 2013, MNRAS, 435, 2152
Kurucz, R. L., Furenlid, I., Brault, J., & Testerman, L. 1984, Solar Flux Atlas from 296 to 1300 nm (Cambridge, MA: Harvard Univ. Press), http://kurucz.harvard.edu/sun/fluxatlas/
Latham, D. W. 1992, in ASP Conf. Ser. 32, IAU Coll. 135: Complementary Approaches to Double and Multiple Star Research, ed. H. A. McAlister & W. I. Hartkopf (San Francisco, CA: ASP), 110
Lindegren, L., Hernández, J., Bombrun, A., et al. 2018, A&A, 616, A2
Lum, M. G., & Boesgaard, A. M. 2019, ApJ, 878, 99
Maderak, R. M., Deliyannis, C. P., King, J. R., & Cummings, J. D. 2013, AJ, 146, 143
Magg, E., Bergemann, M., Serenelli, A., et al. 2022, A&A, 661, A140
Mann, A. W., & von Braun, K. 2015, PASP, 127, 102
Martin, D. C., Fanson, J., Schiminovich, D., et al. 2005, ApJL, 619, L1
Mayor, M. 1985, in IAU Coll. 88: Stellar Radial Velocities, ed. A. G. D. Philip & D. W. Latham (Schenectady, NY: L. Davis Press), 35
Meibom, S., & Mathieu, R. D. 2005, ApJ, 620, 970
Mermilliod, J.-C., Mathieu, R. D., Latham, D. W., & Mayor, M. 1998, A&A, 339, 423
Mermilliod, J.-C., Mayor, M., & Udry, S. 2009, A&A, 498, 949
Mermilliod, J.-C., & Mermilliod, M. 1994, Catalogue of Mean UBV Data on Stars (New York: Springer-Verlag)
Milone, E. F., Schiller, S. J., Mellergaard Amby, T., et al. 2019, AJ, 158, 82
Morrissey, P., Conrow, T., Barlow, T. A., et al. 2007, ApJS, 173, 682
North, P., Studer, M., & Kunzli, M. 1997, A&A, 324, 137
Orosz, J. A., & Hauschildt, P. H. 2000, A&A, 364, 265
Pilachowski, C., Saha, A., & Hobbs, L. M. 1988, PASP, 100, 474
Platais, I. 1991, A&AS, 87, 69
Pribulla, T., Rucinski, S. M., Kuschnig, R., et al. 2009, MNRAS, 392, 847
Pribulla, T., Rucinski, S. M., Latham, D. W., et al. 2010, AN, 331, 397
Rebeirot, E. 1970, A&A, 4, 404
Reddy, A. B. S., Giridhar, S., & Lambert, D. L. 2012, MNRAS, 419, 1350
Ricker, G. R., Winn, J. N., Vanderspek, R., et al. 2015, JATIS, 1, 014003
Rucinski, S. M. 1992, AJ, 104, 1968
Rufener, F. 1988, Catalogue of Stars Measured in the Geneva Observatory Photometric System (4th ed.; Sauverny: Observatoire de Geneve)
Ryan, S. G., & Deliyannis, C. P. 1995, ApJ, 453, 819
Sandquist, E. L., Jessen-Hansen, J., Shetrone, M. D., et al. 2016, ApJ, 831, 11
Sandquist, E. L., Latham, D. W., Shetrone, M. D., et al. 2003, AJ, 125, 810
Schiller, S. J., & Milone, E. F. 1988, AJ, 95, 1466
Schlafly, E. F., Finkbeiner, D. P., Jurić, M., et al. 2012, ApJ, 756, 158
Schönrich, R., McMillan, P., & Eyer, L. 2019, MNRAS, 487, 3568
Sestito, P., Randich, S., & Pallavicini, R. 2004, A&A, 426, 809
Siegel, M. H., LaPorte, S. J., Porterfield, B. L., et al. 2019, AJ, 158, 35
Skrutskie, M. F., Cutri, R. M., Stiening, R., et al. 2006, AJ, 131, 1163
Smalley, B., Kurtz, D. W., Smith, A. M. S., et al. 2011, A&A, 535, A3
Southworth, J. 2015, in ASP Conf. Ser. 496, Living Together: Planets, Host Stars and Binaries, ed. S. M. Rucinski, G. Torres, & M. Zejda (San Francisco, CA: ASP), 164
Spada, F., Demarque, P., Kim, Y.-C., Boyajian, T. S., & Brewer, J. M. 2017, ApJ, 838, 161
Stassun, K. G., Oelkers, R. J., Paegert, M., et al. 2019, AJ, 158, 138
Stassun, K. G., Oelkers, R. J., Pepper, J., et al. 2018, AJ, 156, 102
Stetson, P. B. 1987, PASP, 99, 191
Straižys, V. 1992, Multicolor Stellar Photometry (Tucson, AZ: Pachart Pub. House), http://www.itpa.lt/MulticolorStellarPhotometry/
Taylor, B. J. 2007, AJ, 134, 934
Taylor, B. J., Joner, M. D., & Jeffery, E. J. 2008, ApJS, 176, 262
Telting, J. H., Avila, G., Buchhave, L., et al. 2014, AN, 335, 41
Ter Braak, C. J. F. 2006, Stat. Comput., 16, 239
Tian, Z., Liu, X., Yuan, H., et al. 2020, ApJS, 249, 22
Tody, D. 1986, Proc. SPIE, 627, 733
Tody, D. 1993, in ASP Conf. Ser. 52, Astronomical Data Analysis Software and Systems II, ed. R. J. Hanisch, R. J. V. Brissenden, & J. Barnes (San Francisco, CA: ASP), 173
Torres, G., Andersen, J., & Giménez, A. 2010, A&ARv, 18, 67
Torres, G., Andersen, J., Nordström, B., et al. 2000, AJ, 119, 1942
Torres, G., Clausen, J. V., Bruntt, H., et al. 2012, A&A, 537, A117
Torres, G., Lacy, C. H., Marschall, L. A., et al. 2006, ApJ, 640, 1018
Torres, G., Sandberg Lacy, C. H., Pavlovski, K., et al. 2015, AJ, 150, 154
Tull, R. G. 1998, Proc. SPIE, 3355, 387
Twarog, B. A., Anthony-Twarog, B. J., Deliyannis, C. P., & Thomas, D. T. 2015, AJ, 150, 134
VandenBerg, D. A., Bergbusch, P. A., & Dowler, P. D. 2006, ApJS, 162, 375

Wallace, L., Hinkle, K. H., Livingston, W. C., & Davis, S. P. 2011, ApJS, 195, 6
Williamon, R. M., Sowell, J. R., & Van Hamme, W. 2004, AJ, 128, 1319
Woźniak, P. R., Vestrand, W. T., Akerlof, C. W., et al. 2004, AJ, 127, 2436
Wright, E. L., Eisenhardt, P. R. M., Mainzer, A. K., et al. 2010, AJ, 140, 1868
Zdanavičius, J., Bartašiūtė, D. S., & Zdanavičius, K. 2010, BaltA, 19, 35
Zinn, J. C., Pinsonneault, M. H., Huber, D., et al. 2019, ApJ, 878, 136
Zucker, S., & Mazeh, T. 1994, ApJ, 420, 806